Published in final edited form as:
Nature. 2016 October 20; 538(7625): 406–410. doi:10.1038/nature19794.

Atomic structure of the entire mammalian mitochondrial complex I

Karol Fiedorczuk[1,2], **James A. Letts**[1], **Gianluca Degliesposti**[3], **Karol Kaszuba**[1], **Mark Skehel**[3], and **Leonid A. Sazanov**[1]

[1]Institute of Science and Technology Austria, Klosterneuburg 3400, Austria

[2]MRC Mitochondrial Biology Unit, Cambridge, UK

[3]MRC Laboratory of Molecular Biology, Cambridge, UK

Abstract

Mitochondrial complex I plays a key role in cellular energy production by transferring electrons from NADH to ubiquinone coupled to proton translocation across the membrane1,2. It is the largest protein assembly of the respiratory chain with total mass of 970 kDa3. Here we present a nearly complete atomic structure of ovine mitochondrial complex I at 3.9 Å resolution, solved by cryo-electron microscopy aided by crosslinking/mass-spectrometry mapping. All 14 conserved core and 31 mitochondria-specific supernumerary subunits are resolved within the L-shaped molecule. The hydrophilic matrix arm harbours FMN and 8 iron-sulphur clusters involved in electron transfer, and the membrane arm contains 78 transmembrane helices, mostly contributed by antiporter-like subunits involved in proton translocation. Supernumerary subunits form an interlinked, stabilizing shell around the conserved core. Tightly bound lipids (including cardiolipins) further stabilize interactions between the hydrophobic subunits. Subunits with possible regulatory roles contain additional cofactors, NADPH and two phosphopantetheine molecules, revealed to be involved in inter-subunit interactions. We observe two different conformations of the complex, which may be related to the conformationally driven coupling mechanism and to the active/deactive transition of the enzyme. Our structure provides insight into complex I mechanism, assembly, maturation and dysfunction, allowing detailed molecular analysis of disease-causing mutations.

The electrochemical proton gradient across the inner mitochondrial membrane required by ATP synthase is maintained by the electron transport chain (ETC) proton-pumping complexes I, III and IV1,2. Complex I (CI) is crucial for the entire process and even mild

---

Correspondence and requests for materials should be addressed to L. S. (sazanov@ist.ac.at).

Author Contributions: K.F. purified complex I for grid preparation, prepared cryo-EM grids, acquired and processed EM data, and co-built the models; J.A.L. purified complex I for cross-linking experiments, analysed cross-linking data and co-built the models; G.D. performed cross-linking/mass-spectrometry experiments, K.K. performed model re-building in Rosetta and sequence alignments; G.D. and M.S. analysed cross-linking data; L.A.S. designed and supervised the project, processed and analysed data and wrote the manuscript, with contributions from all authors.

The authors declare no competing financial interests.

Author Information: The EM maps have been deposited in the EMDataBank under accession codes EMD-4084, EMD-4090, EMD-4091 and EMD-4093 (combined map). The model has been deposited in the PDB under accession code 5LNK.

Europe PMC Funders Author Manuscripts

complex I deficiencies can cause severe pathologies4. Mammalian CI is built of 45 (44 unique) subunits. Fourteen “core” subunits, conserved from bacteria, comprise the “minimal” form of the enzyme1,5, an L-shaped structure with seven subunits in the hydrophilic peripheral arm and another seven in the membrane domain. Mammalian complex I also contains 31 “supernumerary” or “accessory” subunits5, forming a shell around the core6. The role of these subunits is unclear. CI likely translocates four protons for every two electrons transferred from NADH to ubiquinone7,8.

CI is the least characterized ETC enzyme. The crystal structure of bacterial (*Thermus thermophilus*) CI is the only full atomic model of the enzyme9–11. In a later structure of the mitochondrial enzyme from aerobic yeast *Yarrowia lipolytica,* the atomic model comprises only about 25% of the protein12. Studies of bovine CI resulted in poly-alanine models for the core and 22 supernumerary subunits6,13. Here we present the nearly complete atomic structure of mammalian complex I, containing all subunits and all known cofactors.

We used the ovine (*Ovis aries*) enzyme (Methods). Classification of cryo-EM images indicated that the relative orientation between the two arms of the complex is variable, producing classes with either an “open” or “closed” angle between them (Extended Data Fig. 1). Particles in the “open” conformation produced a higher resolution map at ~3.9 Å (Extended Data Fig. 2). At the periphery of the molecule the resolution drops (Extended data Fig. 3) due to remaining differences in conformation. Therefore, we performed 3D refinements focused on the peripheral arm (PA) and membrane domain (MD) separately, resulting in more uniformly resolved maps for PA at 3.9 Å resolution and for MD at 4.1 Å (Extended Data Fig. 3). The best maps were combined for model building (Fig. 1a, Extended Data Figs. 3d and 4).

Modelling of the core subunits was facilitated by the conservation of their fold from bacteria6,9. The assignment of the 31 supernumerary subunits (~0.5 MDa) to the remaining density is challenging. To provide experimental verification for previous assignments, to locate remaining subunits and to obtain restraints on the fold of individual subunits, we performed extensive cross-linking/mass-spectrometry mapping experiments (Extended Data Fig. 5, Supplementary Tables). The initial structure was improved by density-guided re-building in Rosetta14, resulting in final model of high quality (Extended Data Fig. 2c).

While this manuscript was under review, a 4.2 Å resolution cryo-EM model for the bovine complex I was published15. The assignments of all subunits agree with our structure, and two major conformations of the complex (somewhat different from ovine) are also observed. However, due to lower resolution the completeness of the atomic model is low for supernumerary subunits (73% of residues are without sidechains) and for the core 51, 24 and 75 kDa subunits (Extended data Tables 1 and 2 in ref15).

In our ovine structure (Fig. 1), subunits were built almost entirely as atomic models with only some surface-exposed loops missing. Subunit B14.7 is disordered, so this area was modelled as poly-alanine according to its clear density in our ovine supercomplex map16. The model is at the atomic level for 88% of the protein (Extended Data Table 1), presenting the most complete atomic structure of mitochondrial complex I to date.

The fold of core subunits is generally conserved from bacteria (Supplementary Discussion). The Fe-S clusters are arranged in the redox chain with distances similar to bovine6 and *T. thermophilus*10 (Fig. 2a). The NADH binding site is also conserved (Fig. 2b), preserving the entire path for electron transfer from NADH towards quinone. Key features in the membrane domain are also conserved, with four proton channels built around the central axis of polar residues propagating from the Q site into the three antiporter-like subunits.

The quinone-binding (Q) site lies at the interface of the hydrophilic 49 kDa/PSST and membrane ND1/ND3 subunits. Throughout we use bovine nomenclature with numbering of residues according to mature17 ovine sequences; see Extended Data Table 1 for human nomenclature. The unique structure of the Q site, which forms an enclosed tunnel extending from the membrane towards cluster N2 about 25 Å away, is conserved with one difference: a loop connecting two strands of the N-terminal β-sheet from the 49 kDa subunit (β1-β2$^{49\text{-kDa}}$ loop) extends further into the cavity, clashing with the position of the bound quinone from the bacterial structure9, where it interacts with conserved His59$^{49\text{-kDa}}$ and Tyr108$^{49\text{-kDa}}$ (Fig. 2c and d). A similar conformation was observed in the yeast enzyme, leading to the proposal that it represents the “deactive” (D) state12. In the absence of substrates, mitochondrial complex I exists in the D state (which may prevent oxygen radical production *in vivo*18) and converts into the “active” (A) state19 only upon turnover. Since in our structure the β1-β2$^{49\text{-kDa}}$ loop will prevent quinone access closer than 20 Å to cluster N2 (blocking electron transfer), it likely also represents the D state. The “closed” conformation resembles one in supercomplex16, so may be more “physiological”. It remains to be established if, as discussed previously12,15, different observed conformations are related to the catalytic cycle or indeed to A/D transitions, but the overall conformational flexibility of the complex is clear.

Supernumerary subunits form a shell around the core subunits6,12, especially around the MD and its interface with the PA. With few exceptions, most supernumerary subunits are not globular, but form extended structures containing α-helices and coils (Extended Data Fig. 6), allowing for numerous interactions at interfaces with other subunits (Extended Data Table 2). They interweave extensively with each other and the core subunits (Extended Data Fig. 7), making the whole mitochondrial complex assembly much more interlinked and thus more stable, with a large total buried surface area (Extended Data Table 2). The intertwined nature of subunit structures suggests that they can be added to the complex only in a certain order, and, therefore, that the assembly of subunits must be tightly controlled20.

The fold of supernumerary subunits is described in the Supplementary Discussion. In summary, those associated with the MD include twelve single TM-helix domain (STMD)21 subunits scattered around the entire domain. Six of these surround the MD tip and contribute their intertwined N-terminal domains to a large matrix “bulge”, the bulk of which is formed by an acyl-carrier protein (ACP)/LYR motif subunit pair (SDAP-β/B22). A large globular 42 kDa subunit from the nucleoside kinase family is attached to the matrix side of ND2 near the PA interface. On the intermembrane space (IMS) side, subunits SGDH and PDSW are “interlocked” *via* their backbone and contain three long α-helices traversing nearly the entire domain (Fig. 1c). PDSW and the subunits with CHCH domains (PGIV, 15 kDa and B18) contain disulphide bonds that further stabilize the fold in the oxidizing environment of the

IMS. PGIV clamps the “heel” of the complex to the middle of the MD. The disulphide-rich, interlocked helices of the IMS subunits, with their rigid and stable structure, appear to replace the hairpin/helix motif (βH) found in bacterial CI9,11.

PA-associated subunits include the NADPH-containing 39 kDa subunit, the Zn-containing 13 kDa subunit and another ACP/LYR pair SDAP-α/B14, with the latter pair and B13 jointly “embracing” the 42 kDa subunit. The PA/MD interface is stabilised by subunit B16.6’s exceptionally long membrane-traversing helix, as well as by B17.2 and B14.5a, both of which contain N-terminal amphipathic α-helices bound at the membrane interface, with the rest of their polypeptides wrapping around hydrophilic arm. Subunits PSST, TYKY and B9 also contain such amphipathic helices, all located at the “heel” of the complex (Fig. 1c), likely assisting in proper PA position over the lipid bilayer.

Several cofactors present in supernumerary subunits are well resolved in the structure (Fig. 3). The 39 kDa subunit is wedged into the side of the PA near the MD interface. It contains a tightly bound non-catalytic NADPH (Fig. 3b) that interacts with conserved $Arg178^{PSST}$, providing a possible mitochondria redox state-sensitive conformational link to cluster N2. In SDAP-α, a phosphopantetheine that is covalently linked to Ser44 extends its attached acyl chain in the “flipped out”22 conformation into the hydrophobic crevice between the helices of the LYR subunit B14 (Fig. 3d). A similar interaction is observed in the SDAP-β/B22 pair. These are the first structures of ACP/LYR complexes showing that their interaction depends on the extended acyl chain and revealing the role of LYR motif. CI is active only when fully assembled with the SDAP-α/B14 pair23. This interaction, which depends on the acyl chain attached to the ACP, may provide a regulatory link between fatty acid synthesis and OXPHOS activity in mitochondria. The 13 kDa subunit harbours a Zn-binding motif, coordinating a Zn^{2+} ion in the vicinity of clusters N6a and N5. Zn-containing proteins are sensitive to oxidative stress24, and loss of the 13 kDa subunit leads to loss of cluster N6a25, as it becomes exposed. In this way CI may be equipped with an oxidative stress “sensor”, in addition to bound NADPH.

Twelve bound lipids were identified in crevices between hydrophobic subunits. Several observed lipid molecules have four acyl chains and were therefore assigned as cardiolipins, known to be essential for activity26. Strikingly, a cardiolipin (CDL1, Fig. 3a) and three other lipid molecules fill the void left by the missing (in metazoans) three ND2 N-terminal helices6. This void is encircled by the 2-TM helix subunit B14.5b and the STMD subunit KFYI, hinting that the ND2 helices may have been lost in evolution to accommodate a specific binding site for lipids. Two cardiolipins (CDL2/3) fill a large gap between the antiporter-like ND4 and ND5 subunits, preventing potential proton leaks and instability. Another cardiolipin (CDL4) stabilizes amphipathic helices at the “heel” of the complex. The structure thus shows the basis for the essential role of cardiolipin and other lipids.

The mechanism of coupling between electron transfer and proton translocation is still enigmatic. Conservation of key features from bacteria to mammals suggests that the basic mechanism is likely the same, with add-on “stabilisers” and “regulators”. As we proposed earlier9, the central axis of polar residues in the membrane probably plays a key role (Fig. 4a). In each catalytic cycle, the negative charge stored either on Q or on nearby residues in

the enclosed Q site may drive conformational changes in ND1 and the proton channel near the Q site, which would propagate *via* the central axis to channels in antiporter-like subunits ND2, ND4 and ND5, resulting in changes of pKa and accessibility of key residues. The net result would be the pumping of four protons per cycle, one per each channel. The observed conformation of loops in the Q site likely reflects the D state. This conformation might also occur during normal function when quinol is ejected from the site into the lipid bilayer, if A/D transitions are related to conformations encountered during the catalytic cycle12. Supernumerary subunits implicated in A/D transitions (39 kDa, B13 and SDAP-α/B14 pair) could also participate in catalytic conformational changes by interacting with the key TM1-$TM2^{ND3}$ loop flanking the Q site, and possibly through interactions with the 42 kDa subunit (Fig. 4b). In the "closed" class, B13 and SDAP-α move towards 42 kDa (Extended Data Fig. 8), hinting at such a possibility. Since the 42 kDa subunit is metazoan-specific27, its role may be to "fine tune" movements during turnover. The traverse helix HL from ND5 appears to play mainly a stabilizing "stator" role28 rather than being a moving element29. Rigid disulphide-rich supernumerary subunits traversing the IMS side of the membrane domain may represent another "stator" element unique to the mitochondrial enzyme (Fig. 4b).

Our structure clearly shows that supernumerary subunits stabilize the complex. Some of them, especially those containing additional cofactors (39 kDa, SDAPs, B14, B22 and 13 kDa) and phosphorylated residues (42 kDa, ESSS, MWFE, B14.5a, B14.5b and B16.6)30, may provide regulatory links to the redox status of the cell, lipid biosynthesis and mitochondrial homeostasis. Known human pathological mutations are present in all core and many supernumerary subunits4. Our structure provides the framework for understanding the molecular basis of mutations and mechanisms of complex I function and regulation.

Methods

Data reporting

No statistical methods were used to predetermine sample size. The experiments were not randomized. The investigators were not blinded to allocation during experiments and outcome assessment.

Protein purification and electron microscopy

Protein was purified from *Ovis aries* heart mitochondria following the protocol adapted with some modifications from a previously published procedure for the bovine enzyme32,33. We explored *Ovis aries* as a source of complex I that may be more suitable for high resolution structural studies than the extensively studied bovine enzyme. We find that ovine enzyme appears more stable, as it is highly active after purification and retains the 42 kDa subunit, easily lost from bovine complex33. In terms of overall sequence similarity ovine is as good a model of the human enzyme as bovine (~84%)33. All 44 different subunits of complex I were identified in the preparation by mass-spectrometry33. Briefly, fresh ovine hearts were purchased from the local abattoir and mitochondria prepared as described previously32. Mitochondrial membranes were solubilized in the branched chain detergent Lauryl Maltose Neopentyl Glycol (LMNG, 1%) and the sample applied to Q-sepharose HP anion exchange column (GE Healthcare) equilibrated with 20 mM Tris-HCl, pH 7.4, 10% (v/v) glycerol, 1

mM EDTA, 1 mM DTT and 0.1% LMNG. Protein was eluted with a NaCl gradient, peak fractions concentrated and applied to Superose 6 HiLoad 16/60 column equilibrated in 20 mM HEPES, pH 7.4, 2 mM EDTA, 1.5% (v/v) glycerol, 100 mM NaCl and 0.02% Brij-35. The peak fraction was concentrated to ~5 mg/ml protein and ~0.2% Brij-35. Then 2.7 μl of sample was applied to glow discharged Quantifoil R 0.6/1 copper grids and blotted for 34s at 90% humidity in the chamber of FEI Vitrobot IV. Immediately after sample was snap frozen in liquid ethane. Extensive trials with different detergents, including previously used Cymal-76, revealed Brij-35 as the detergent giving the most homogeneous spread of particles. Imaging was performed with a 300 kV Titan Krios electron microscope equipped with direct electron detector FEI Falcon-II (ETH Zurich, ScopeM center) in automated data collection mode at a calibrated magnification of 1.39 Å $pixel^{-1}$ (100,720 X) and dose of 26 e s^{-1} $Å^{-2}$ with total 3 s exposure time. The data were collected as seven movie frames fractionated over the first second of exposure and an averaged image over 3 seconds.

Image processing

We collected a total of 2.6k micrographs in two datasets, which were combined. All processing steps were done using RELION34 unless otherwise stated. We used averaged images from high dose 3 s exposure for initial CTF estimations using CTFFIND435 and for automated particle picking in Relion, resulting in ~241k particles. MOTIONCORR36 was used for whole-image drift correction of movie frames 1-7 (1 s) of each micrograph. Contrast transfer function (CTF) parameters of the corrected micrographs were estimated using Gctf and refined locally for each particle37. The particles were extracted using 296^2 pixel box and sorted by reference-free 2D classification, resulting in ~171k particles selected from good 2D classes. These were used for 3D classification with a regularization parameter T of 8 and a 30 Å low-pass filtered initial model from a previous low resolution model of the bovine enzyme6. That resulted in ~130k particles of good quality; however, it was clear that the relative orientation between the two arms of the complex is slightly variable, producing 3D classes with either an “open” or “closed” angle between the arms (Extended Data Fig. 1). Particles in the “open” conformation (~82k particles) produced higher resolution maps and were selected for a final reconstruction. For all high-resolution refinements, particles were reextracted from the motion corrected micrographs with a 512^2 pixel box to allow for high-resolution CTF correction38. After initial auto-refinement, particle-based beam-induced motion correction and radiation-damage weighing (particle polishing) was performed39.

Refinement of polished particles gave a map resolved to 3.9 Å. All resolutions are based on the gold-standard (two halves of data refined independently) Fourier shell correlation (FSC) = 0.143 criterion40. This 3D class selection probably still allows for small variations in the conformation, therefore the local resolution varies within the map, especially at the extremities of both arms (Extended Data Fig. 3). At the periphery of the molecule the resolution drops not only due to the usual decrease in the precision of particle alignments in these areas, but also due to differences in the protein conformation, greatest at the edges of the molecule. To overcome this limitation we performed 3D refinement focused on the peripheral and membrane domains separately (with the subtraction of signal from the remaining parts of the complex41). This resulted in a 3.9 Å map of the peripheral arm (PA), very well resolved in all areas, including the edges of the domain. The membrane domain

(MD) refined to 4.1 Å, however, the map was more uniform and so better resolved for the distal part of the domain (near subunit ND5) as compared to the density from the refinement of the entire complex (Extended data Fig. 3). Higher quality refinement of the peripheral arm probably stems from the fact that high electron density of 8 Fe-S clusters helps in particle alignment. The least ordered part of the complex is the 42 kDa subunit, loosely attached to the membrane domain. We have performed extended 3D classification of the "open" class in order to identify the most homogeneous population, especially with respect to 42 kDa subunit. This class (64k particles) was refined to 4.0 Å, and the resulting density was used to model the 42 kDa subunit. To assist with overall model building and refinement, several maps were carved around specific parts of the complex and combined into one map in UCSF Chimera42: peripheral arm from PA-focused refinement, the area around ND4/5 subunits (tip of the membrane domain) from MD-focused refinement, the 42 kDa subunit density as above, and the rest of the complex from the overall 3.9 Å map for the "open" class (Fig. 1a and Extended Data Fig. 3). The final model was refined against this combined map.

The final map is of high quality, with about three-quarters of the map at 3.9 Å resolution and the rest at 4.1 Å. Large- and medium-size side chains, as well as relatively small Val and Thr, are clearly seen in the density (Extended Data Fig. 4). Carboxylates (Asp, Glu) have much lower density than other residues owing to early radiation damage, as observed previously43. Disulphide bridges also are subject to early damage, as in X-ray crystallography44. Few features at the interfaces of maps used for the combined map may be better resolved in individual maps, since in overlapping regions both maps contribute. For example, the β1-$\beta 2^{49\text{-kDa}}$ loop is better resolved in the PA-focused map, which is deposited along with other constituent maps. Overall map filtered to lower resolution is very similar to the previous 5 Å resolution map for the bovine enzyme6, suggesting that the mammalian complex I structure is very well conserved. One difference is that in ovine complex the accessory 4TM subunit B14.7 is disordered in the detergent used for the microscopy samples (Brij-35). It is likely to be disordered rather than detached as B14.7 was identified by mass-spectrometry in the sample used for EM (data not shown). Since Brij-35 gave us the best yield of particles, we kept its use for data collection, but took advantage of the availability of cryo-EM maps of ovine respiratory supercomplexes in our lab. In these maps all the subunits of complex I are well ordered, and so in our final complex I model we included the poly-ALA model of B14.7 based on 5.8 Å resolution map of the "tight" respirasome16. Loss of B14.7 also results in the disorder of the nearby C-terminal half of traverse helix HL and TM16 from ND5, as well as TM4 from ND6, which were also modeled as poly-alanine (these stretches can be recognized by B-factor set to 200) based on the "tight" respirasome map. The register in poly-alanine stretches is approximate. The density for the 42 kDa subunit is rather weak but this subunit clearly preserves the nucleoside kinase family fold, which allowed us to model most of it using Rosetta and visible large side-chains as a guide.

Model building and refinement

For the 14 core subunits the initial homology models were generated manually based on the *T. thermophilus* structure9 with side-chains rebuilt to ovine sequence using SQWRL4 software45. Homology models were generated with Phyre246 and Swiss-model47 servers for all supernumerary subunits, although they were mostly useful only for subunits with

large globular domains, such as the 42 kDa and 39 kDa subunits, as well as for those with known structure of close homologues (SDAP's and B8). Secondary structure predictions for all subunits were generated with PredictProtein48, PsiPred49 and TMHMM50 servers, and were helpful during model building. Initial assignments of the location and the fold of supernumerary subunits were based on our cross-linking data and the secondary structure features and side-chain density observed in the cryo-EM map, with checks for consistency with the knowledge on subcomplexes and assembly intermediates in complex I. The initial models were adjusted to cryo-EM density (in cases when homology models were useful) or built manually in COOT51. Lipids were tentatively assigned on the basis of appearance in the density as cardiolipins, phosphatidylcholines and phosphatidylethanolamines, known to co-purify with the complex26,52.

Initial models were re-built and refined in Rosetta release version 2016.02.58402 using protocols optimized for cryo-EM maps14. For each subunit, 100 different models were produced in Rosetta with optimization of density fit using *elec_dens_fast* function (with –*denswt* = 40, chosen from several trials), selection of the best fitting structure and structure relaxation using –*FastRelax* flag. From the produced structures several best-scoring by density fit and geometry were selected and used in COOT to guide further model building/optimization. This procedure resulted mainly in improvements to backbone geometry, especially in coils, still allowing for the good fit of side-chains into density.

After several rounds of re-building the final model was refined with the Phenix suite53 phenix.real_space_refine program for 5 macro-cycles using the electron scattering table with default and secondary structure restrains. This resulted in high quality model in terms of geometry (Molprobity score 2.5, i.e. corresponding to average structure at 2.5 Å resolution) and fit to density (Extended Data Fig. 2c).

Cross-linking

All the cross-linking reactions were performed using purified solutions of Complex I at a concentration of 1 mg/ml. Following experimental optimisation, ten separate experiments were performed. Experiments varied in relation to the detergent added to the buffer (DDM, LMNG or LDAO/DDM), the cross-linking reagent (targeting lysine or acidic residues) and the protease used to digest the samples (trypsin or endoproteinase Glu-C) (Supplementary Table 1).

Isotopically labelled cross-linking reagents were purchased from Creative Molecules (Canada). 4-(4,6-dimethoxy-1,3,5-triazin-2-yl)-4-methylmorpholinium chloride (DMTMM) was purchased from Sigma. Homobifunctional, isotopically-coded N-HydroxySuccinimide (NHS) esters disuccidinimidyl suberate (DSS H_{12}/D_{12}), bis-sulphodisuccinimidyl suberate (BS3 H_{12}/D_{12}) and disuccinimidyl adipate (DSA $^{12}C_6/^{13}C_6$) were used at a final concentration of 50 μM as cross-linking reagents to target lysine residues. The reactions were incubated for 45 min at 37 °C and quenched by adding NH_4HCO_3 to a final concentration of 50 mM and incubating for further 15 min. Isotopically labeled adipic acid dihydrazide (ADH H_8/D_8) and suberic acid dihydrazide (SDH H_{12}/D_{12}) were used to target the acidic residues, using DMTMM as catalyst. The cross-linking reaction was initiated by adding ADH or SDH and DMTMM to final concentrations 5 mg ml^{-1}, 6 mg ml^{-1} and 12 mg

ml^{-1} respectively. The samples were incubated at 37 °C for 60 min and the reactions stopped using gel filtration (Zeba Spin Desalting columns 7K MWCO).

The cross-linked samples were freeze-dried and then resuspended in 50mM NH_4HCO_3, 8M Urea and 0.1% SDS to a final concentration of 1 mg ml^{-1}. Size exclusion protein fractionation was performed through a Superdex 200 Increase 3.2/300 column (GE Healthcare) with 50mM NH_4HCO_3, 8M Urea and 0.1% SDS as mobile phase at a flow rate of 25 µl min^{-1}. Two-minute fractions were collected and their protein content evaluated by SDS-PAGE. Fractions of similar content were pooled into 4-5 main fractions and concentrated to 1 mg ml^{-1} using Amicon Ultra-0.5 mL Centrifugal Filters (Millipore).

The filtered cross-linked samples were then enzymatically digested. Samples were freeze-dried and resuspended in 50mM NH_4HCO_3 and 8M Urea to a final protein concentration of 1 mg ml^{-1}, reduced with 10mM DTT and alkylated with 50 mM iodoacetamide. Following alkylation, samples were diluted with 50 mM NH_4HCO_3 to 1 M urea prior to trypsin digestion (or 2 M for Glu-C digestion). Trypsin and Glu-C were added at an enzyme-to-substrate ratio of 1:20 and 1:100 respectively. Digestions were carried out overnight at 37 °C and 25 °C for trypsin and Glu-C respectively. After digestion, the samples were acidified with formic acid to a final concentration of 2% v/v and the peptides fractionated by peptide size exclusion chromatography, using a Superdex Peptide 3.2/300 (GE Healthcare) with 30% v/v Acetonitrile/0.1% v/v TFA as mobile phase and at a flow rate of 50 µl/min. Fractions were collected every 2 min over the elution volume 1.0 ml to 1.7 ml. Prior to LC-MS/MS analysis fractions were freeze dried and resuspended in 2% v/v acetonitrile and 2% v/v formic acid.

The digests were analysed by nano-scale capillary LC-MS/MS using an Ultimate U3000 HPLC (ThermoScientific Dionex, San Jose, USA) to deliver a flow of approximately 300 nL/min. A C18 Acclaim PepMap100 5 μm, 100 μm x 20 mm nanoViper (ThermoScientific Dionex, San Jose, USA), trapped the peptides prior to separation on a C18 Acclaim PepMap100 3 μm, 75 μm x 250 mm nanoViper (ThermoScientific Dionex, San Jose, USA). Peptides were eluted with a gradient of acetonitrile. The analytical column outlet was directly interfaced via a nano-flow electrospray ionisation source, with a hybrid dual pressure linear ion trap mass spectrometer (Orbitrap Velos, ThermoScientific, San Jose, USA). Data dependent analysis was carried out, using a resolution of 30,000 for the full MS spectrum, followed by ten MS/MS spectra in the linear ion trap. MS spectra were collected over a m/z range of 300–2000. MS/MS scans were collected using threshold energy of 35 for collision-induced dissociation.

For data analysis, Xcalibur raw files were converted into the open mzXML format through MSConvert (Proteowizard) with a 32-bit precision. mzXML files were directly used as input for xQuest searches on a local xQuest installation54. The selection of cross-linked precursor MS/MS data was based on the following criteria: a mass difference among the heavy and the light cross-linker of: 12.07532 Da for BS3, DSS and SDH, 6.02016 Da for DSA and 8.05016 Da for ADH; precursor charge ranging from 3+ to 8+; maximum retention time difference 2.5 min. Searches were performed against an ad-hoc database containing all the sequences of Ovine complex I subunits together with their reverse used as decoy database.

The following parameters were set for xQuest searches: maximum number of missed cleavages (excluding the cross-linking site) 3; peptide length 4–50 amino acids; fixed modifications carbamidomethyl-Cys (mass shift 57.02146 Da); mass shift of the light cross-linker 138.06808 Da for DSS and BS3, 138.0906 Da for ADH, 110.03675 for DSA and 166.1218 for SDH; mass shift of mono-links 156.0786 and 155.0964 Da for DSS and BS3, 138.0906 Da for ADH, 127.0628 Da and 128.0468 Da for DSA, and 184.1324 Da for SDH; MS1 tolerance 10 ppm, MS2 tolerance 0.2 Da for common ions and 0.3 for cross-link ions; search in enumeration mode (exhaustive search). Search results were filtered according to the following criteria: MS1 mass tolerance window −3 to 7 ppm. Finally each MS/MS spectra was manually inspected and validated.

In total 218 unique cross-linked peptides were identified, of which 87 were between residues of different subunits (inter-subunit, Supplementary Table 2), 73 were between residues within the same subunit (intra-subunit, Supplementary Table 3), and 58 were clear false positives (Supplementary Table 4). False positives were identified by comparison to all known biochemical and structural information on complex I and the cross-links that are considered false positives are either between residues that are too distant from each other (>32 Å after allowing for exposed side chain flexibility from their modeled position), located on opposite sides of the membrane or the reactive residues are buried and not solvent accessible in the intact structure. Many of the false positive cross-links are found on unstructured coils at the edges of the complex I structure indicating that they likely result from transient interactions between different molecules of complex I during the reaction (inter-complex cross-links). True positive cross-links were more likely to be observed in more than one experiment. Some high-scoring cross-links were observed between disordered termini or loops of subunits that could not be modeled in our structure, hence the accurate determination of distance for these cross-links was not possible. Nonetheless in cases where cross-linking residues are adjacent to the modeled regions, the cross-links were considered true and are included in Extended Data Fig. 5 and Supplementary Tables 2 and 3. No cross-links were observed for any of the mitochondrially encoded core subunits, which are buried in the membrane and coated with a layer of supernumerary subunits. Good quality cross-links were observed for all supernumerary subunits expect for B14.7, KFYI and AGGG. These data in conjunction with our EM maps allowed us to unambiguously assign all supernumerary subunits. Previous assignments were confirmed and importantly, subunits that previously had no known position in the complex (10 kDa, B14.5a, MWFE, B9, MNLL, SGDH, ASHI, B17, AGGG and B12) have now been assigned and built (see Supplementary Discussion for more details).

Europe PMC Funders Author Manuscripts

Extended Data

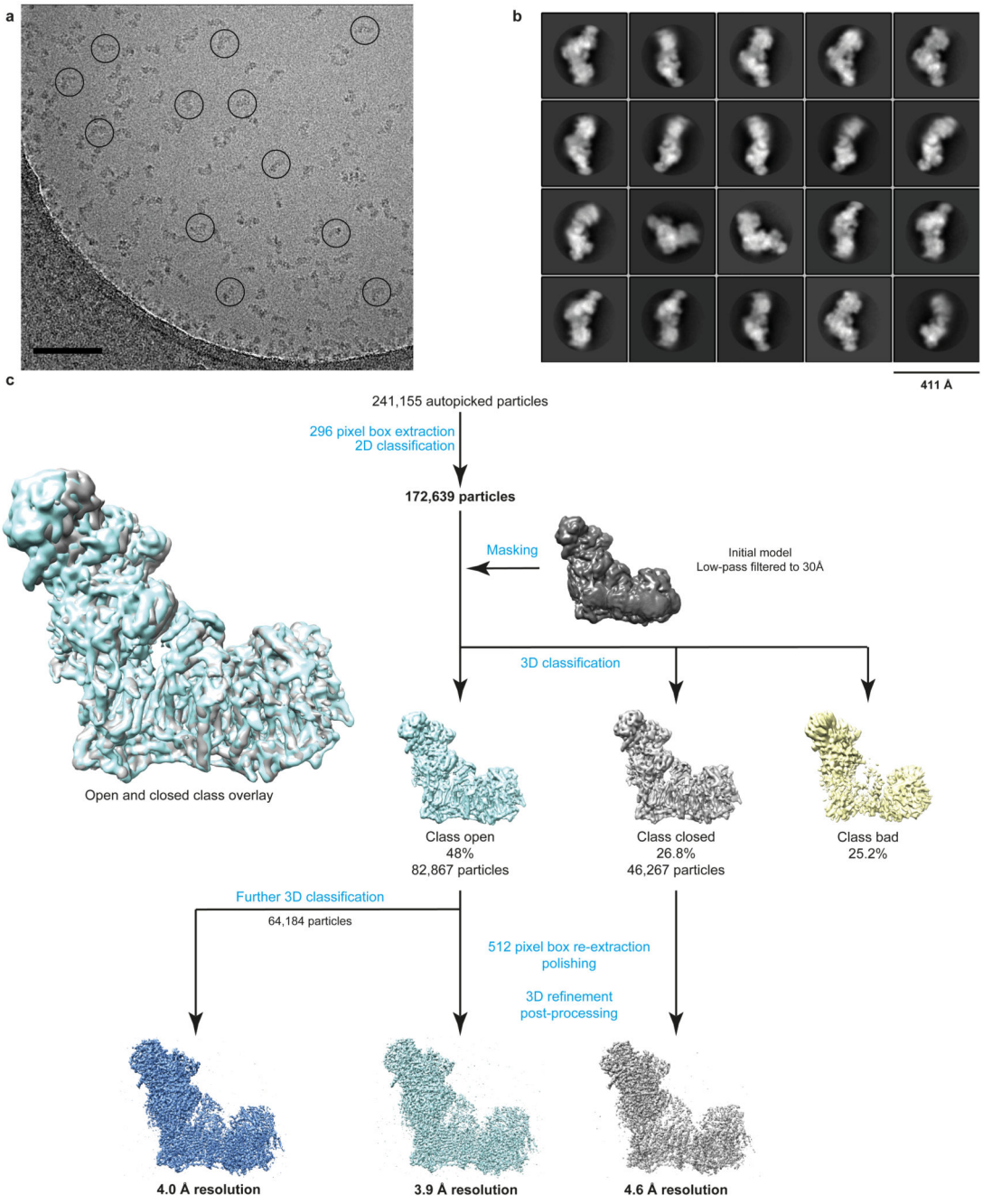

Extended Data Figure 1. Image processing procedures.

a. Representative micrograph of 2.6k micrographs collected which all varied somewhat in defocus, ice thickness and particle count, with good quality particles circled. Scale bar = 100 nm. **b.** Representative 2D class averages obtained from reference-free classification. **c.** Classification and refinement procedures used in this study.

Europe PMC Funders Author Manuscripts

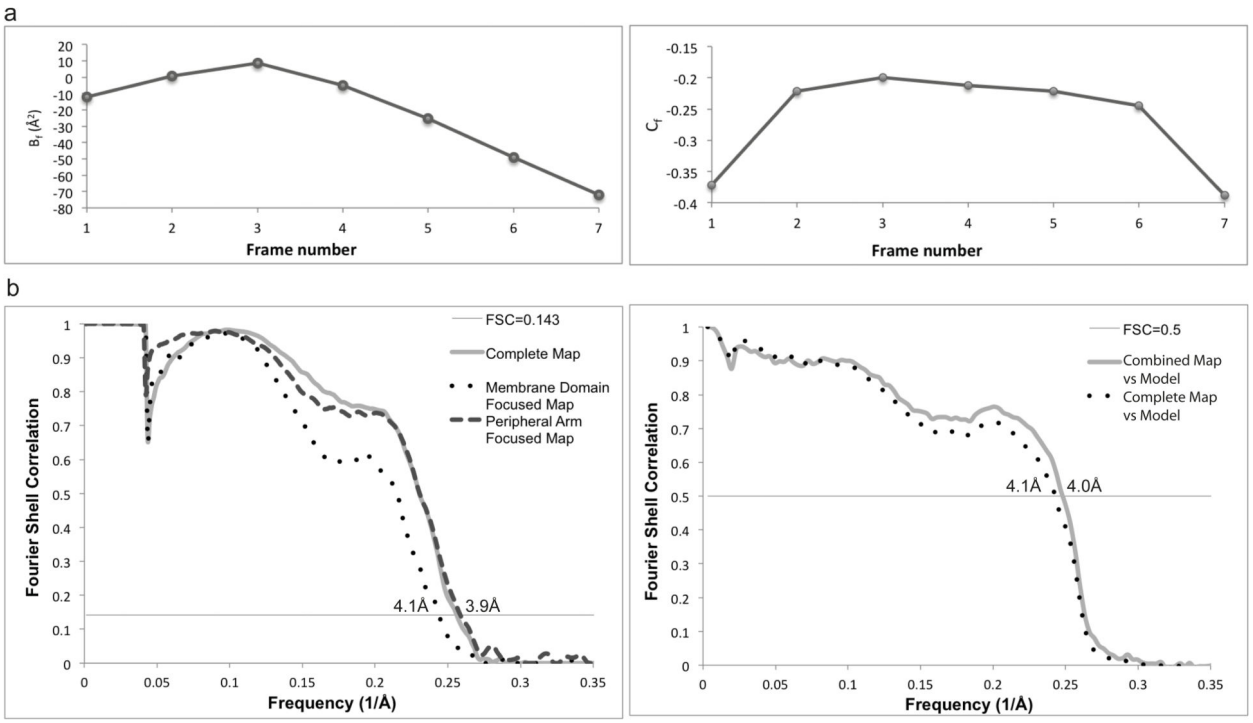

c. Statistics

Data collection				
EM	Titan Krios 300kV, FEI Falcon II			
Pixel size (Å)	1.39			
Defocus range (μm)	-0.5 to -3.5			
Reconstruction (RELION)	Overall	Membrane Domain	Peripheral Arm	64k class (for 42kDa)
Accuracy of rotations (°)	0.573	0.711	0.728	0.591
Accuracy of translations (pixel)	0.308	0.400	0.400	0.325
B-factor from post-processing	-88	-85	-83	-89
B-factor for map visualisation	-100	-150	-100	-120
Final resolution (Å)	3.9	4.1	3.9	4.0
Model refinement (PHENIX)	Complete model			
Resolution limit (Å)	3.9			
Number of residues	8037			
Map CC (whole unit cell)	0.758			
Map CC (around atoms)	0.782			
Rmsd (bonds)	0.009			
Rmsd (angles)	1.04			
Average B-factor	86.0			
Validation				
All-atom clashscore	24.4			
Ramachandran plot				
Outliers (%)	0.5			
Allowed (%)	12.5			
Favoured (%)	87.0			
Rotamer outliers (%)	0.1			
Molprobity score	2.5			

Extended Data Figure 2. Image and model refinement procedures.

a. Radiation-damage weighting. Relative B-factors (B_f) and intercepts (C_f) from the Relion particle polishing procedure. **b.** Left, gold-standard (two halves of data refined independently) FSC curves for the maps of the entire complex complete map (resolution at FSC = 0.143 is 3.9 Å), membrane domain (MD) focused refinement (4.1 Å resolution) and peripheral arm (PA) focused refinement (3.9 Å resolution). Right, FSC curve of the combined map *vs* final model shows good agreement of the model with the map (FSC=0.5 at

Europe PMC Funders Author Manuscripts

4.0 Å resolution). FSC curve against the entire complex complete map, which was not used in refinement, is shown as a control. **c.** Statistics of refinement.

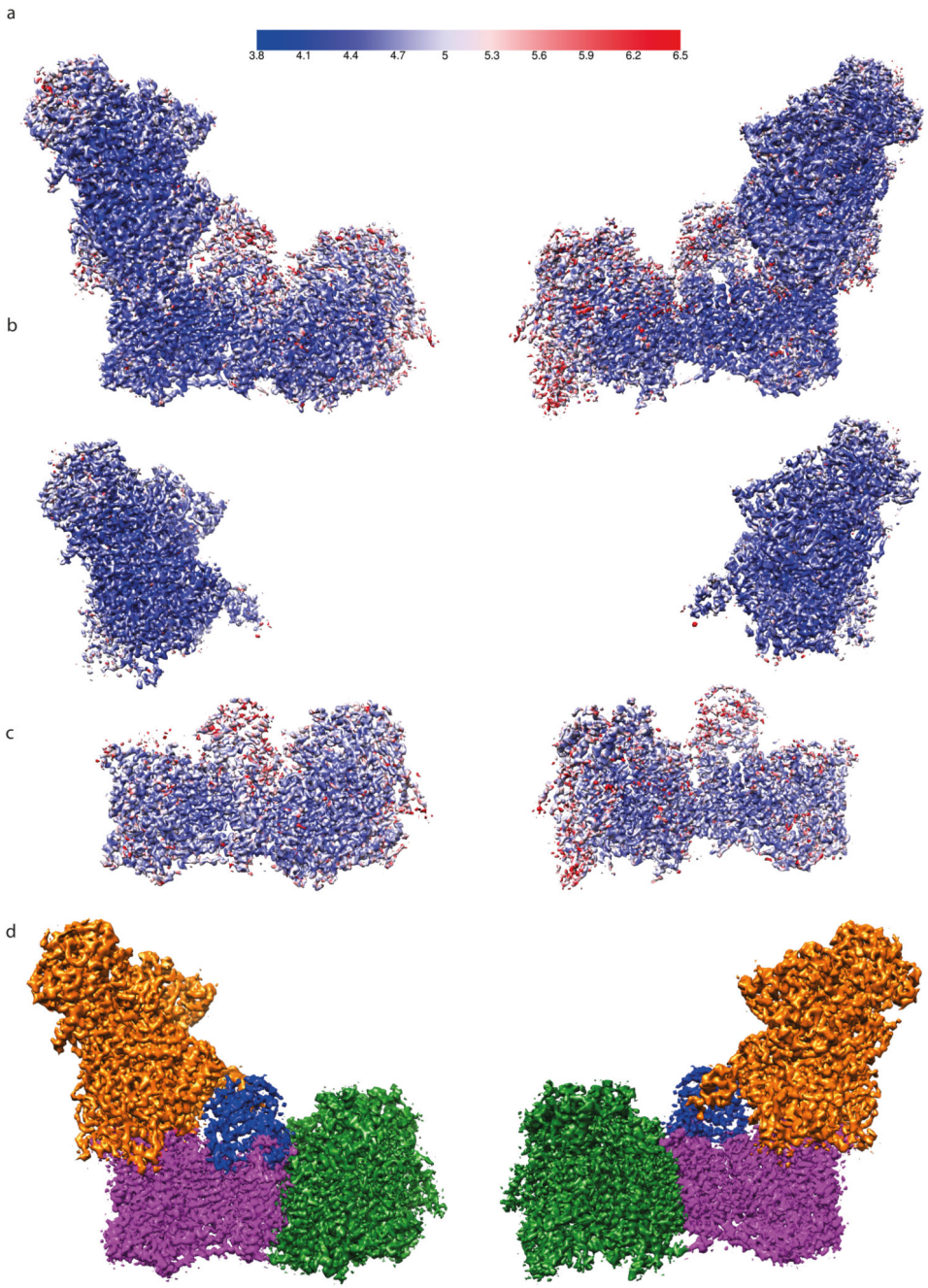

Extended Data Figure 3. Local resolution estimation and combination of maps for model building.

Local resolution estimation by Resmap of **a**. entire complex I, **b.** peripheral arm focused refinement map and **c**. membrane domain focused refinement map. Maps are coloured according to the shown resolution scale in Å. **d.** The final map was produced by combining maps with the best local resolution features, i.e. for peripheral arm – PA focused refinement

map (orange), for the distal part of membrane domain – MD focused refinement map (green), for 42 kDa subunit – map from the selected homogenous complex I class (64k particles; blue) and the rest of the complex from the best map of the entire complex (magenta).

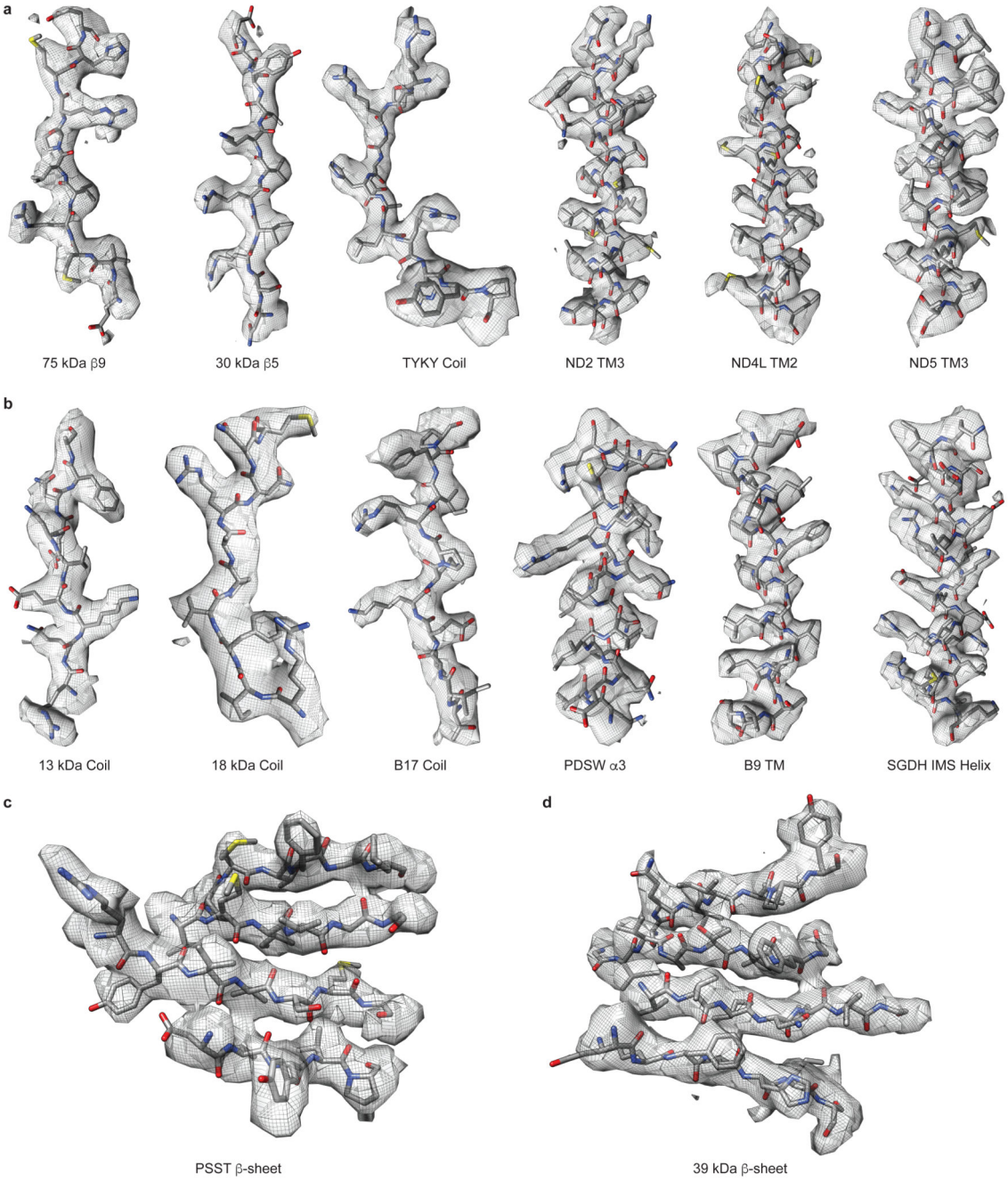

Extended Data Figure 4. Examples of cryo-EM density.

Coils and α-helices from **a.** core and **b.** supernumerary subunits. Example β-sheets from **c.** core PSST subunit and **d.** supernumerary 39 kDa subunit. Cryo-EM density is shown with

Europe PMC Funders Author Manuscripts

the model represented as sticks and coloured by atom with carbon grey, oxygen red, nitrogen blue and sulphur yellow.

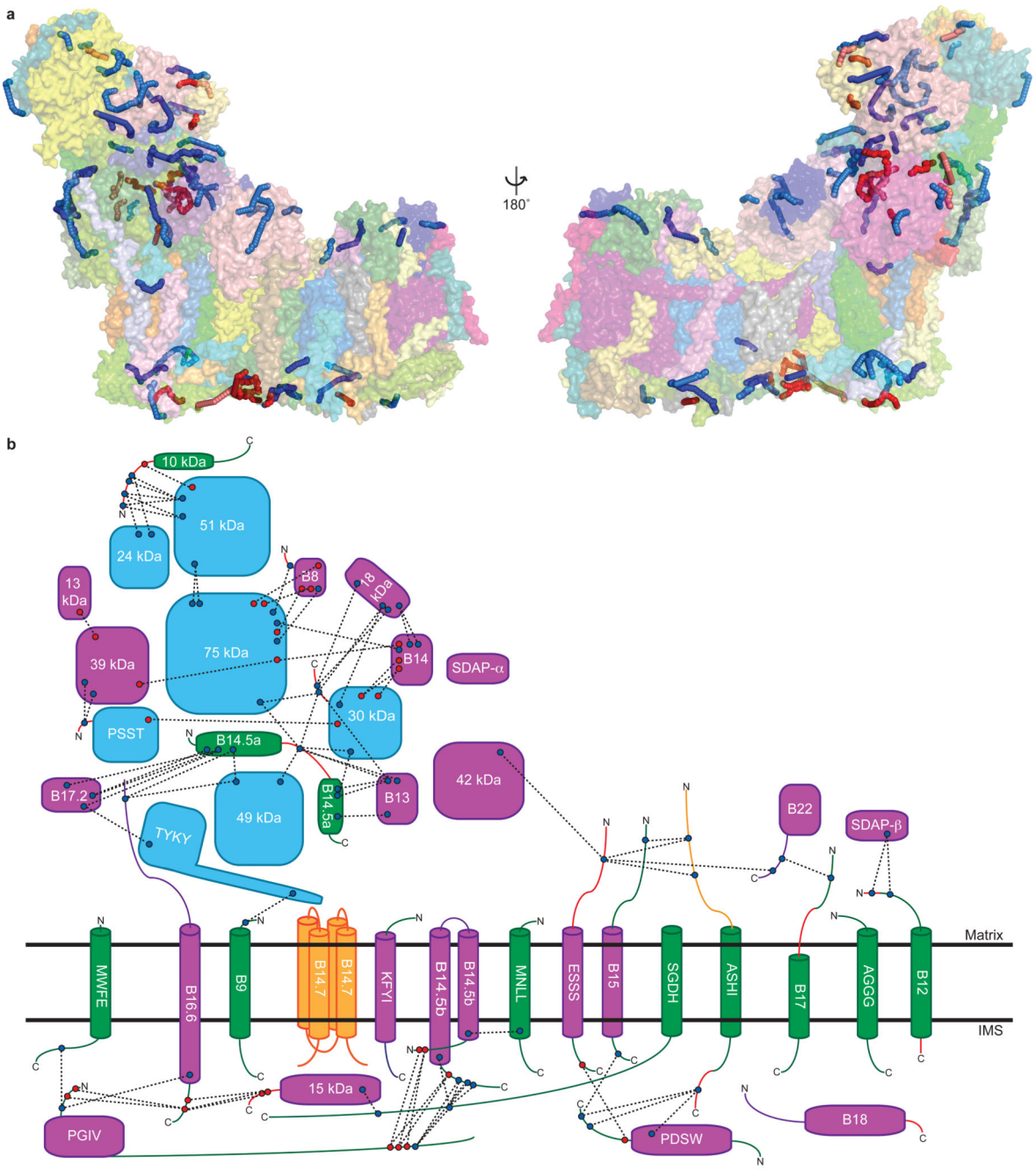

Extended Data Figure 5. Identified cross-links.

a. Solvent accessible surface (SAS) representation of cross-links. Surfaces for complex I subunits are shown transparent and coloured as in Fig. 1. Shortest (SAS) paths calculated using Xwalk55 are shown for cross-links as coloured worms with inter-subunit lysine reactive cross-links in blue, inter-subunit acid reactive cross-links in red, intra-subunit lysine

Europe PMC Funders Author Manuscripts

reactive cross-links in light blue, intra-subunit acid reactive cross-links in light red. **b.** Inter-subunit cross-link schematic. Complex I subunits are shown in a similar orientation as in **a.** left panel with core subunits cyan, previously assigned supernumerary subunits in magenta, newly assigned or newly built regions of supernumerary subunits in green, poly-alanine regions in orange and unmodelled regions in red. Observed cross-links are indicated by dashed black lines between either blue circles (lysine reactive cross-links) or red circles (acid reactive cross-links). No cross-links were observed to the core subunits of the membrane arm and hence they were omitted for clarity. The horizontal black lines indicate the approximate boundaries of the IMM. Subunits B14.7, B15 and ASHI are shown as being behind the membrane boundaries as they are found on the opposite (far) side of the membrane arm.

Europe PMC Funders Author Manuscripts

Europe PMC Funders Author Manuscripts

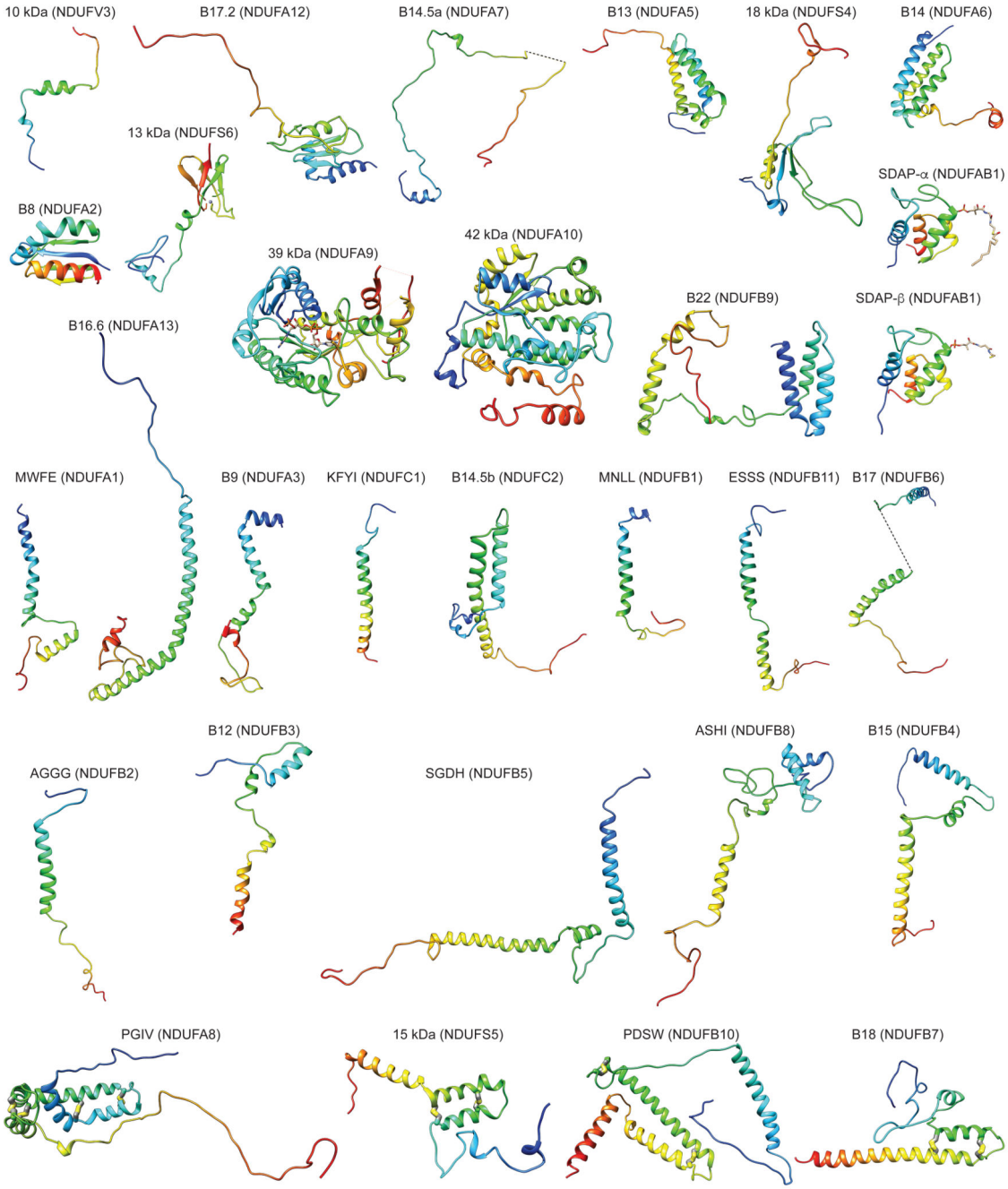

Extended Data Figure 6. Folds of supernumerary subunits.

Subunits are shown in cartoon representation, coloured blue to red from N- to C-terminus. Disulphide bridges are shown as sticks with sulphur in yellow.

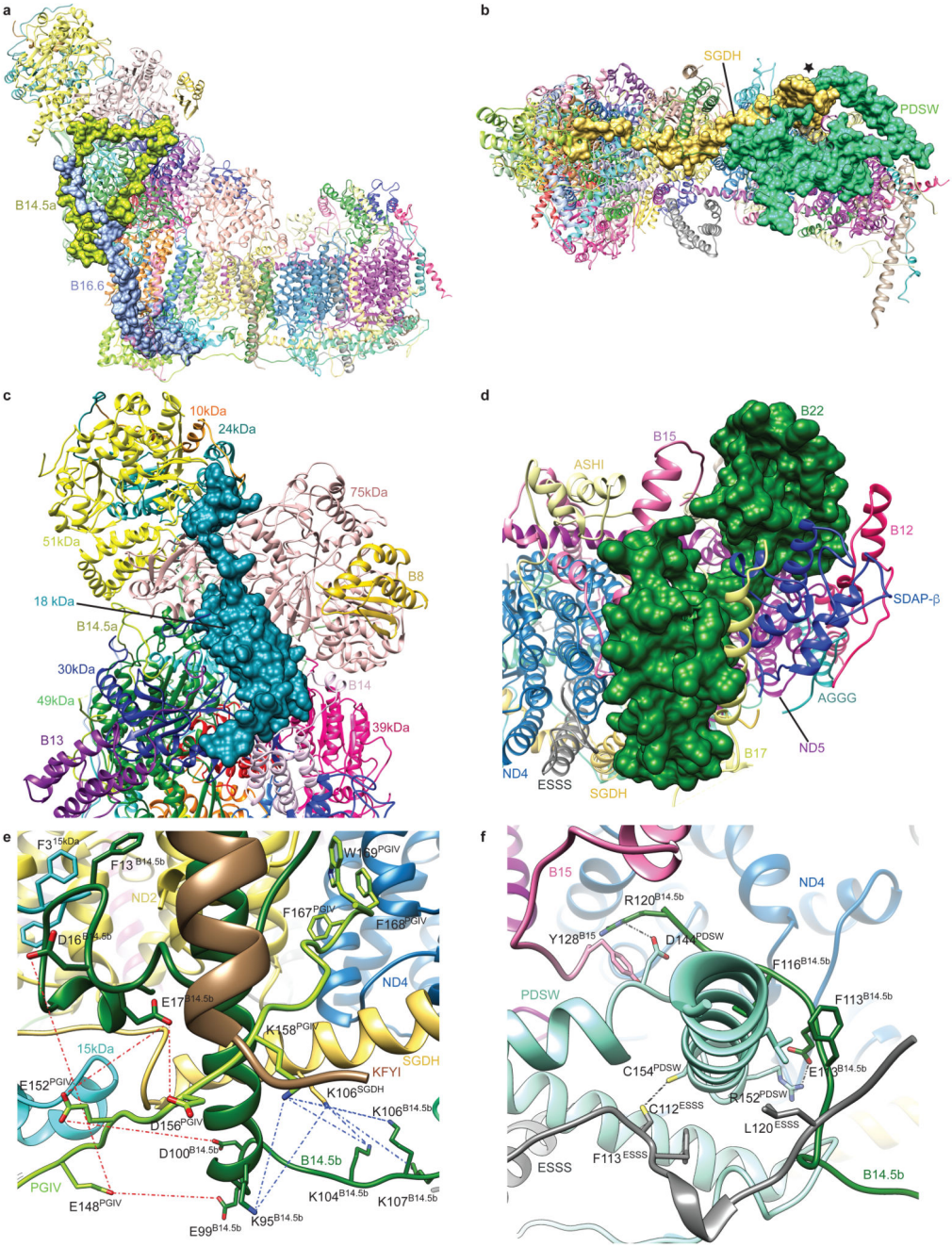

Extended Data Figure 7. Examples of supernumerary subunits interactions.

a. Side view of complex I showing surfaces for subunits B14.5a and B16.6. **b.** IMS view of complex I showing surfaces for subunits SGDH and PDSW. The point at which the two subunits are intertwined is marked with a star. **c.** View of the hydrophilic arm looking from above the membrane arm. The surface of the 18 kDa subunit which spans the hydrophilic arm is shown. **d.** Matrix view of the tip of the membrane arm with the surface of supernumerary subunit B22 shown. **e.** Close up of the centre of the membrane arm on the IMS side. This region contains many interactions between supernumerary subunits and the

side chains of residues involved are shown. The region is also a hot spot for cross-links, the side chains involved are shown and cross-links are indicated with dashed lines (acid cross-links: red; basic cross-links: blue). **f.** Close up of the C-terminal helix of supernumerary subunit PDSW at the centre of the membrane arm on the IMS side. This helix extends away from complex I and is encircled by the C-termini of supernumerary subunits B14.5b, ESSS and B15. The side chains of residues involved in stabilizing interactions are shown. A possible disulphide bond between PDSW (Cys154) and ESSS (Cys112) and stabilizing salt-bridges are indicated by dashed lines. Subunits are coloured as in Fig. 1.

Europe PMC Funders Author Manuscripts

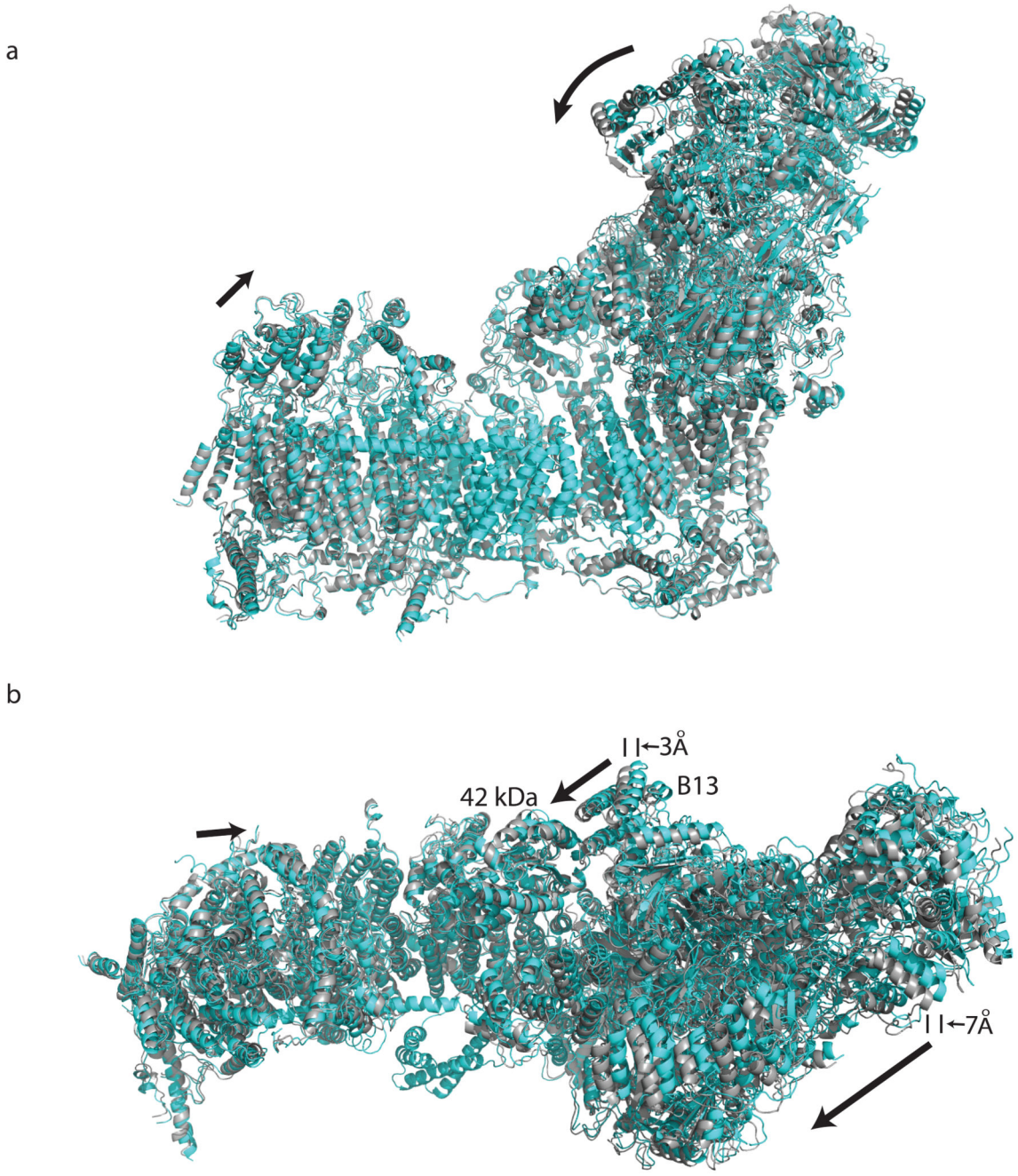

Extended Data Figure 8. Comparison of "open" and "closed" 3D class structures.

a. Side and **b**. top view from the matrix for the alignment of the "open" class structure (in cyan) and "closed" class structure (in gray). To generate the closed class structure, the final structure of the "open" class was refined in real space in Phenix (5 macro cycles with morphing at each cycle) against 4.6 Å map of the "closed" class (Extended Data Fig. 1). All the α-helices were well fit into density, but due to low resolution of the "closed" class no further refinement was performed and the comparison of structures involves only the relative positions of secondary structure elements. The two structures were aligned via TM core

subunits and are displayed as cartoon models. In the “closed” class the peripheral arm undergoes a hinge-like motion around the Q site towards the tip of the membrane domain, with the direction of shift indicated by the arrow in **b**. As a result, subunit B13 moves ~3 Å closer to the 42 kDa subunit, allowing for direct contacts. The shift is larger at the periphery, reaching 7 Å at the tip of the peripheral arm. Additionally, subunit ND5 and its matrix “bulge” move about 3 Å towards peripheral arm.

Extended Data Table 1
Summary of the model.

	Subunit Name Bovine / Human	Chain	Total residues / range built	Poly-ALA model	Un-modelled residues	% atomic model	TMHs	Cofactors / N
Core	51kDa / NDUFV1	1	445 / 7-438	-	1-6, 439-445	97.1	-	FMN N3 (4Fe[5
	24kDa / NDUFV2	2	217 / 3-216	-	1-2, 217	98.6	-	N1a (2Fe[2
	75kDa / NDUFS1	3	704 / 6-693	-	1-5, 694-704	97.7	-	N1b (2Fe[7 N4 (4Fe[75 N5 (4Fe[75
	49kDa / NDUFS2	4	430 / 44-430	-	1-43	90.0	-	-
	30kDa / NDUFS3	5	228 / 7-214	-	1-6, 215-228	91.2	-	-
	PSST / NDUFS7	6	179 / 25-179	-	1-24	86.6	-	N2 (4Fe[P
	TYKY / NDUFS8	9	176 / 1-176	-	-	100	-	N6a (4Fe[T N6b (4Fe[T
	ND1	H	318 / 1-318	-	-	100	8	
	ND2	N	347 / 1-347	-	-	100	11	(antiporter-l
	ND3	A	115 / 1-115	-	-	100	3	
	ND4	M	459 / 1-459	-	-	100	14	(antiporter-l
	ND4L	K	98 / 1-86	-	87-98	87.8	3	
	ND5	L	606 / 1-568	509-598	599-606	84.0	16	(antiporter-l
	ND6	J	175 / 1-108, 123-175	77-122	-	73.7	5	-
Supernumerary	10kDa / NDUFV3	a	75 / 34-74	-	1-33, 75	54.7	-	-
	13kDa / NDUFS6	b	96 / 1-95	-	96	99.0	-	Zn^{2+}
	18kDa / NDUFS4	c	133 / 11-133	-	1-10	92.5	-	-
	39kDa / NDUFA9	d	345 / 1-252, 277-338	325-338	253-276, 339-345	87.0	-	NADPH
	B8 / NDUFA2	e	98 / 13-96	-	1-12, 97-98	85.7	-	Thioredoxin
	B13 / NDUFA5	f	115 / 4-115	-	1-3	97.4	-	-
	B14 / NDUFA6	g	127 / 14-127	-	1-13	89.8	-	LYR prote
	B14.5a / NDUFA7	h	112 / 1-71, 89-112	-	72-88	84.8	-	-
	B17.2 / NDUFA12	i	145 / 1-144	-	145	99.3	-	-
	SDAP-α / NDUFAB1	j	88/ 3-87	-	1-2, 88	96.6	-	Acyl carrier p phosphopante
	42kDa / NDUFA10	k	320 / 1-320	227-320	-	70.9	-	Nucleoside kinas

Subunit Name Bovine / Human	Chain	Total residues / range built	Poly-ALA model	Un-modelled residues	% atomic model	TMHs	Cofactors / N
15kDa / NDUFS5	l	105 / 1-95	-	96-105	90.5	-	Quadruple CX CHCH dom
B9 / NDUFA3	m	83 / 4-83	-	1-3	96.4	1	STMD
B12 / NDUFB3	n	97 / 13-86	83-86	1-12, 87-97	73.2	1	STMD
B14.5b / NDUFC2	o	120 / 1-120	-	-	100	2	-
B15 / NDUFB4	p	128 / 17-73, 95-128	17-27, 74-94	1-16	62.5	1	STMD
B16.6 / NDUFA13	q	143 / 4-143	-	1-3	97.9	1	Identical to GR STMD
B17 / NDUFB6	r	127 / 1-37, 63-118	63-71	38-62, 119-127	66.1	1	STMD
B18 / NDUFB7	s	136 / 5-122	5-15	1-4, 123-136	78.7	-	Double Cx_9C domain
B22 / NDUFB9	t	178 / 9-174	-	1-8, 175-178	93.3	-	LYR prote
AGGG / NDUFB2	u	72 / 3-68	-	1-2, 69-72	91.7	1	STMD
ASHI / NDUFB8	v	158 / 1-84, 101-143	1-100	144-158	27.2	1	STMD
ESSS / NDUFB11	w	125 / 38-123	-	1-37, 124-125	68.8	1	STMD
KFYI / NDUFC1	x	49 / 1-48	-	49	98.0	1	STMD
MNLL / NDUFB1	y	57 / 4-56	-	1-3, 57	93.0	1	STMD
MWFE / NDUFA1	z	70 / 2-70	-	1	98.6	1	STMD
PDSW / NDUFB10	Z	175 / 3-173	-	1-2, 174-175	97.7	-	-
PGIV / NDUFA8	Y	171 / 1-171	-	-	100	-	Quadruple CX CHCH dom
SDAP-β / NDUFAB1	X	88 / 1-88	-	-	100	-	Acyl carrier p phosphopante
SGDH / NDUFB5	W	143 / 5-143	-	1-4	97.2	1	STMD
B14.7 / NDUFA11	V	140 / 7-125	7-125	21	0	4	-
Total		8516 / 8037	518	479	88.3	78	

Extended Data Table 2

Summary of interactions between subunits of ovine complex I.

Subunit	Surface area, Å^2	Buried area, Å^2	ΔG^{int} kcal/mol	N_{HB}	N_{SB}	Interacting subunits (Descending buried area order, core subunits in bold)
Entire complex summary						
	297384.9	259150.4	-1838.5			
Core subunits						
51kDa	19017.7	6988.3	-12.38	77	18	**24kDa, 75kDa**, 10kDa, 18kDa, B14.5a
24kDa	14271.6	5144.8	-34.27	43	15	**51kDa**, 10kDa, **75kDa**, 18kDa, 13kDa

Subunit	Surface area, Å^2	Buried area, Å^2	ΔG^{int} kcal/mol	N_{HB}	N_{SB}	Interacting subunits (Descending buried area order, core subunits in bold)
75kDa	29733.9	10317.9	-23.97	102	43	18kDa, **51kDa**, B8, **49kDa**, **24kDa, 30kDa**, B17.2, B14, **TYKY**, 13kDa, B14.5a, 39kDa, 10kDa
49kDa	17459.5	11703.0	-39.24	93	37	**30kDa, TYKY, PSST**, B14.5a, **ND1**, B16.6, **75kDa**, B13, **ND3**, 13kDa, B14
30kDa	14832.7	9972.2	-40.37	79	34	**49kDa**, B13, 18kDa, B14.5a B14 **PSST, 75kDa**, 39kDa, **TYKY**
PSST	9483.5	6258.3	-26.86	47	31	**49kDa, ND1, TYKY, 30kDa**, 39kDa, **ND3**, B17.2, B14
TYKY	13499.4	10446.6	-47.00	87	33	**49kDa**, B17.2, **PSST**, B14.5a, 13kDa, **ND1, 75kDa**, B16.6, B9, **30kDa**, 18kDa, 39kDa, MWFE
ND1	16976.8	11161.2	-98.77	61	21	**ND3**, MWFE, **PSST, 49kDa, ND6**, B16.6, **TYKY**, B9, PGIV, B17.2
ND2	16531.5	9336.0	-106.34	19	1	**ND4L**, 42kDa, **ND4**, B14.5b, 15kDa, **ND5**, SGDH
ND3	10944.8	6994.6	-81.41	15	0	**ND1, ND6, ND4L, PSST**, 49kDa, B9, 39kDa, B14, B16.6
ND4	18758.1	11100.2	-98.26	42	3	**ND5**, ESSS, **ND2**, B15, SGDH, MNLL, PDSW, B22, PGIV, B14.5b, ASHI
ND4L	6435.4	4638.4	-64.53	7	2	**ND6, ND2**, 15kDa, ND3
ND5	26832.2	10837.8	-94.45	47	5	**ND4**, AGGG, B22, PDSW, ASHI, B17, B18, B12, B15, **ND2**, SDAP-β , SGDH, B14.7
ND6	12734.4	8272.0	-95.71	19	2	**ND4L, ND3, ND1**, 15kDa, B16.6, MWFE
Supernumerary subunits						
10kDa	4892.2	2471.0	-15.11	23	9	**51kDa, 24kDa**, 18kDa, **75kDa**
13kDa	7651.1	2991.2	-10.11	16	6	**TYKY**, B17.2, 39kDa, **75kDa, 49kDa, 24kDa**
18kDa	11083.8	5848.7	-11.52	57	20	**75kDa, 30kDa**, B14, 51kDa, 39kDa, 10kDa, **TYKY, 24kDa**, B17.2
39kDa	16659.0	3814.3	-5.70	20	11	**PSST**, 13kDa, **30kDa**, B14, 18kDa, **ND3, 75kDa, TYKY**
B8	5628.2	1196.4	-2.44	13	10	**75kDa**
B13	8653.4	2370.0	-15.60	14	5	**30kDa, 49kDa**, B14.5a
B14	9627.2	4586.9	-9.29	31	19	SDAP-α, **30kDa**, 18kDa, **75kDa**, 39kDa, **ND3, 49kDa, PSST**
B14.5a	11473.6	5753.0	-40.33	49	17	**49kDa, 30kDa, TYKY, 75kDa**, B17.2, B13, B16.6, **51kDa**
B17.2	12313.0	4593.5	-25.36	40	9	**TYKY**, 13kDa, **75kDa**, B14.5a, **PSST, ND1**, 18kDa
SDAP-α	5667.7	731.3	-3.93	7	12	B14
SDAP-β	6074.4	2554.8	-9.23	22	26	B22, B17, B12, **ND5**, AGGG

Subunit	Surface area, Å^2	Buried area, Å^2	ΔG^{int} kcal/mol	N_{HB}	N_{SB}	Interacting subunits (Descending buried area order, core subunits in bold)
42kDa	16761.9	1942.1	-19.89	2	0	**ND2**, KFYI, B14.5b
15kDa	9228.8	5236.4	-29.49	27	9	SGDH, B16.6, **ND2, ND6, ND4L**, PGIV, B14.5b
B9	8142.1	3420.4	-27.55	19	8	PGIV, **ND1**, B16.6, **TYKY, ND3**, SGDH
B12	7188.3	2427.6	-13.38	14	7	**ND5**, AGGG, SDAP-β , B22
B14.5b	10935.4	5873.6	-39.62	31	8	**ND2**, KFYI, PDSW, SGDH, PGIV, **ND4**, 15kDa, ESSS, 42kDa, B15
B15	10929.5	3772.9	-15.63	16	0	**ND4**, ASHI, B22, **ND5**, PDSW, B14.5b
B16.6	14451.0	7839.8	-51.27	42	12	PGIV, 15kDa, ND1, **49kDa**, **ND6**, MWFE, B9, **TYKY**, B14.5a, **ND3**, SGDH
B17	10137.0	4528.8	-24.39	29	6	B22, PDSW, **ND5**, B18, SDAP-β , SGDH
B18	9860.6	3512.3	-6.33	24	6	**ND5**, AGGG, ASHI, B17, PDSW
B22	14868.0	5662.9	-32.67	25	15	**ND5**, B17, SDAP-β , B15, SGDH, B12, **ND4**, ASHI
AGGG	7273.2	3125.3	-26.86	17	7	**ND5**, B18, B12, SDAP-β , ASHI
ASHI	11797.4	2971.5	-22.74	10	1	B15, **ND5**, B18, **ND4**, AGGG, B22
ESSS	8835.5	4764.1	-39.36	21	5	**ND4**, PDSW, SGDH, B14.5b
KFYI	5365.5	1349.6	-12.98	0	2	B14.5b, 42kDa
MNLL	5714.8	1719.4	-14.42	9	5	**ND4**, SGDH, PDSW
MWFE	6638.2	3788.4	-29.68	29	4	**ND1**, PGIV, B16.6, **ND6, TYKY**
PDSW	15770.6	7444.1	-35.07	54	8	ESSS, SGDH, **ND5**, B17, B14.5b, **ND4**, B18, B15, MNLL
PGIV	14545.4	6552.6	-38.16	49	28	B16.6, B9, MWFE, SGDH, B14.5b, 15kDa, **ND4, ND1**
SGDH	14101.4	8031.0	-55.12	40	10	**ND4**, PDSW, 15kDa, ESSS, B14.5b, MNLL, PGIV, B22, **ND2**, B17, **ND5**, B16.6, B9

Analysis was performed using the PISA server (www.ebi.ac.uk/pdbe/pisa/).

ΔG_{int} indicates the solvation free energy gain upon formation of the assembly, N_{HB} – number of hydrogen bonds at the interface and N_{SB} – number of salt bridges at the interface.

Supplementary Material

Refer to Web version on PubMed Central for supplementary material.

Acknowledgements

We thank the ETH Zurich ScopeM center for access to Titan Krios EM. Data processing was performed at the IST high-performance computer cluster. K.F. is partially funded by the Medical Research Council UK PhD fellowship. J.A.L. holds a long-term fellowship from FEBS.

References

1. Sazanov LA. A giant molecular proton pump: structure and mechanism of respiratory complex I. Nat Rev Mol Cell Biol. 2015; 16:375–388. [PubMed: 25991374]
2. Moser CC, Farid TA, Chobot SE, Dutton PL. Electron tunneling chains of mitochondria. Biochim Biophys Acta. 2006; 1757:1096–1109. [PubMed: 16780790]
3. Letts JA, Sazanov LA. Gaining mass: the structure of respiratory complex I-from bacterial towards mitochondrial versions. Curr Opin Struct Biol. 2015; 33:135–145. [PubMed: 26387075]
4. Fassone E, Rahman S. Complex I deficiency: clinical features, biochemistry and molecular genetics. J Med Genet. 2012; 49:578–590. [PubMed: 22972949]
5. Walker JE. The NADH - ubiquinone oxidoreductase (complex I) of respiratory chains. Q Rev Biophys. 1992; 25:253–324. [PubMed: 1470679]
6. Vinothkumar KR, Zhu J, Hirst J. Architecture of mammalian respiratory complex I. Nature. 2014; 515:80–84. [PubMed: 25209663]
7. Galkin A, Drose S, Brandt U. The proton pumping stoichiometry of purified mitochondrial complex I reconstituted into proteoliposomes. Biochim Biophys Acta. 2006; 1757:1575–1581. [PubMed: 17094937]
8. Wikstrom M, Sharma V, Kaila VR, Hosler JP, Hummer G. New perspectives on proton pumping in cellular respiration. Chem Rev. 2015; 115:2196–2221. [PubMed: 25694135]
9. Baradaran R, Berrisford JM, Minhas GS, Sazanov LA. Crystal structure of the entire respiratory complex I. Nature. 2013; 494:443–448. [PubMed: 23417064]
10. Sazanov LA, Hinchliffe P. Structure of the hydrophilic domain of respiratory complex I from *Thermus thermophilus*. Science. 2006; 311:1430–1436. [PubMed: 16469879]
11. Efremov RG, Sazanov LA. Structure of the membrane domain of respiratory complex I. Nature. 2011; 476:414–420. [PubMed: 21822288]
12. Zickermann V, et al. Structural biology. Mechanistic insight from the crystal structure of mitochondrial complex I. Science. 2015; 347:44–49. [PubMed: 25554780]
13. Zhu J, et al. Structure of subcomplex Iβ of mammalian respiratory complex I leads to new supernumerary subunit assignments. Proc Natl Acad Sci USA. 2015; 112:12087–12092. [PubMed: 26371297]
14. DiMaio F, et al. Atomic-accuracy models from 4.5-A cryo-electron microscopy data with density-guided iterative local refinement. Nat Meth. 2015; 12:361–365.
15. Zhu J, Vinothkumar KR, Hirst J. Structure of mammalian respiratory complex I. Nature. 2016; 536:354–58. [PubMed: 27509854]
16. Letts JA, Fiedorczuk K, Sazanov LA. Architecture of Respiratory Supercomplexes. Nature. 2016 In press.
17. Carroll J, Fearnley IM, Shannon RJ, Hirst J, Walker JE. Analysis of the subunit composition of complex I from bovine heart mitochondria. Mol Cell Proteomics. 2003; 2:117–126. [PubMed: 12644575]
18. Chouchani ET, et al. Cardioprotection by S-nitrosation of a cysteine switch on mitochondrial complex I. Nat Med. 2013; 19:753–759. [PubMed: 23708290]
19. Vinogradov AD, Grivennikova VG. The mitochondrial complex I: progress in understanding of catalytic properties. IUBMB Life. 2001; 52:129–134. [PubMed: 11798024]
20. Sanchez-Caballero L, Guerrero-Castillo S, Nijtmans L. Unraveling the complexity of mitochondrial complex I assembly: A dynamic process. Biochim Biophys Acta. 2016; 1857:980–990. [PubMed: 27040506]
21. Zickermann V, Angerer H, Ding MG, Nubel E, Brandt U. Small single transmembrane domain (STMD) proteins organize the hydrophobic subunits of large membrane protein complexes. FEBS Lett. 2010; 584:2516–2525. [PubMed: 20398659]
22. Cronan JE. The chain-flipping mechanism of ACP (acyl carrier protein)-dependent enzymes appears universal. Biochem J. 2014; 460:157–163. [PubMed: 24825445]
23. Angerer H. Eukaryotic LYR Proteins Interact with Mitochondrial Protein Complexes. Biology. 2015; 4:133–150. [PubMed: 25686363]

24. Oteiza PI. Zinc and the modulation of redox homeostasis. Free Rad Biol Med. 2012; 53:1748–1759. [PubMed: 22960578]
25. Kmita K, et al. Accessory NUMM (NDUFS6) subunit harbors a Zn-binding site and is essential for biogenesis of mitochondrial complex I. Proc Natl Acad Sci USA. 2015; 112:5685–5690. [PubMed: 25902503]
26. Sharpley MS, Shannon RJ, Draghi F, Hirst J. Interactions between phospholipids and NADH:ubiquinone oxidoreductase (complex I) from bovine mitochondria. Biochemistry. 2006; 45:241–248. [PubMed: 16388600]
27. Brandt U. Energy converting NADH:quinone oxidoreductase (complex I). Annu Rev Biochem. 2006; 75:69–92. [PubMed: 16756485]
28. Belevich G, Knuuti J, Verkhovsky MI, Wikstrom M, Verkhovskaya M. Probing the mechanistic role of the long alpha-helix in subunit L of respiratory Complex I from Escherichia coli by site-directed mutagenesis. Mol Microbiol. 2011; 82:1086–1095. [PubMed: 22060017]
29. Efremov RG, Baradaran R, Sazanov LA. The architecture of respiratory complex I. Nature. 2010; 465:441–445. [PubMed: 20505720]
30. Palmisano G, Sardanelli AM, Signorile A, Papa S, Larsen MR. The phosphorylation pattern of bovine heart complex I subunits. Proteomics. 2007; 7:1575–1583. [PubMed: 17443843]
31. Berrisford JM, Sazanov LA. Structural basis for the mechanism of respiratory complex I. J Biol Chem. 2009; 284:29773–29783. [PubMed: 19635800]
32. Sazanov LA, Peak-Chew SY, Fearnley IM, Walker JE. Resolution of the membrane domain of bovine complex I into subcomplexes: implications for the structural organization of the enzyme. Biochemistry. 2000; 39:7229–7235. [PubMed: 10852722]
33. Letts JA, Degliesposti J, Fiedorczuk K, Skehel M, Sazanov LA. Purification of Ovine Respiratory Complex I Results in a Highly Active and Stable Preparation. 2016 Submitted.
34. Scheres SH. RELION: implementation of a Bayesian approach to cryo-EM structure determination. J Struct Biol. 2012; 180:519–530. [PubMed: 23000701]
35. Rohou A, Grigorieff N. CTFFIND4: Fast and accurate defocus estimation from electron micrographs. J Struct Biol. 2015; 192:216–221. [PubMed: 26278980]
36. Li X, et al. Electron counting and beam-induced motion correction enable near-atomic-resolution single-particle cryo-EM. Nat Meth. 2013; 10:584–590.
37. Zhang K. Gctf: Real-time CTF determination and correction. J Struct Biol. 2016; 193:1–12. [PubMed: 26592709]
38. Rosenthal PB, Henderson R. Optimal Determination of Particle Orientation, Absolute Hand, and Contrast Loss in Single-particle Electron Cryomicroscopy. J Mol Biol. 2003; 333:721–745. [PubMed: 14568533]
39. Scheres SH. Beam-induced motion correction for sub-megadalton cryo-EM particles. Elife. 2014; 3:e03665. [PubMed: 25122622]
40. Scheres SH, Chen S. Prevention of overfitting in cryo-EM structure determination. Nat Meth. 2012; 9:853–854.
41. Bai XC, Rajendra E, Yang G, Shi Y, Scheres SH. Sampling the conformational space of the catalytic subunit of human γ-secretase. Elife. 2015; 4:e11182. [PubMed: 26623517]
42. Pettersen EF, et al. UCSF chimera - A visualization system for exploratory research and analysis. J Comput Chem. 2004; 25:1605–1612. [PubMed: 15264254]
43. Allegretti M, Mills DJ, McMullan G, Kuhlbrandt W, Vonck J. Atomic model of the F420-reducing [NiFe] hydrogenase by electron cryo-microscopy using a direct electron detector. Elife. 2014; 3:e01963. [PubMed: 24569482]
44. Meents A, Gutmann S, Wagner A, Schulze-Briese C. Origin and temperature dependence of radiation damage in biological samples at cryogenic temperatures. Proc Natl Acad Sci USA. 2010; 107:1094–1099. [PubMed: 20080548]
45. Krivov GG, Shapovalov MV, Dunbrack RL Jr. Improved prediction of protein side-chain conformations with SCWRL4. Proteins. 2009; 77:778–795. [PubMed: 19603484]
46. Kelley LA, Mezulis S, Yates CM, Wass MN, Sternberg MJ. The Phyre2 web portal for protein modeling, prediction and analysis. Nat Protoc. 2015; 10:845–858. [PubMed: 25950237]

47. Biasini M, et al. SWISS-MODEL: modelling protein tertiary and quaternary structure using evolutionary information. Nucleic Acids Res. 2014; 42:W252–258. [PubMed: 24782522]
48. Rost B, Yachdav G, Liu J. The PredictProtein server. Nucleic Acids Res. 2004; 32:W321–326. [PubMed: 15215403]
49. McGuffin LJ, Bryson K, Jones DT. The PSIPRED protein structure prediction server. Bioinformatics. 2000; 16:404–405. [PubMed: 10869041]
50. Krogh A, Larsson B, von Heijne G, Sonnhammer EL. Predicting transmembrane protein topology with a hidden Markov model: application to complete genomes. J Mol Biol. 2001; 305:567–580. [PubMed: 11152613]
51. Emsley P, Cowtan K. Coot: model-building tools for molecular graphics. Acta Crystallogr. 2004; D 60:2126–2132.
52. Shinzawa-Itoh K, et al. Bovine heart NADH-ubiquinone oxidoreductase contains one molecule of ubiquinone with ten isoprene units as one of the cofactors. Biochemistry. 2010; 49:487–492. [PubMed: 19961238]
53. Adams PD, et al. PHENIX: a comprehensive Python-based system for macromolecular structure solution. Acta Crystallogr. 2010; D66:213–221.
54. Leitner A, Walzthoeni T, Aebersold R. Lysine-specific chemical cross-linking of protein complexes and identification of cross-linking sites using LC-MS/MS and the xQuest/xProphet software pipeline. Nat Protoc. 2014; 9:120–137. [PubMed: 24356771]
55. Kahraman A, Malmstrom L, Aebersold R. Xwalk: computing and visualizing distances in cross-linking experiments. Bioinformatics. 2011; 27:2163–2164. [PubMed: 21666267]
56. Bridges HR, Bill E, Hirst J. Mossbauer spectroscopy on respiratory complex I: the iron-sulfur cluster ensemble in the NADH-reduced enzyme is partially oxidized. Biochemistry. 2012; 51:149–158. [PubMed: 22122402]
57. Carroll J, Ding S, Fearnley IM, Walker JE. Post-translational modifications near the quinone binding site of mammalian complex I. J Biol Chem. 2013; 288:24799–24808. [PubMed: 23836892]
58. Page CC, Moser CC, Chen X, Dutton PL. Natural engineering principles of electron tunnelling in biological oxidation-reduction. Nature. 1999; 402:47–52. [PubMed: 10573417]
59. Birrell JA, Morina K, Bridges HR, Friedrich T, Hirst J. Investigating the function of [2Fe-2S] cluster N1a, the off-pathway cluster in complex I, by manipulating its reduction potential. Biochem J. 2013; 456:139–146. [PubMed: 23980528]
60. Verkhovskaya ML, Belevich N, Euro L, Wikstrom M, Verkhovsky MI. Real-time electron transfer in respiratory complex I. Proc Natl Acad Sci USA. 2008; 105:3763–3767. [PubMed: 18316732]
61. Galkin A, et al. Identification of the mitochondrial ND3 subunit as a structural component involved in the active/deactive enzyme transition of respiratory complex I. J Biol Chem. 2008; 283:20907–20913. [PubMed: 18502755]
62. Lazarou M, Thorburn DR, Ryan MT, McKenzie M. Assembly of mitochondrial complex I and defects in disease. Biochim Biophys Acta. 2009; 1793:78–88. [PubMed: 18501715]
63. Szklarczyk R, et al. NDUFB7 and NDUFA8 are located at the intermembrane surface of complex I. FEBS Lett. 2011; 585:737–743. [PubMed: 21310150]
64. Herrmann JM, Riemer J. Mitochondrial disulfide relay: redox-regulated protein import into the intermembrane space. J Biol Chem. 2012; 287:4426–4433. [PubMed: 22157015]
65. Fearnley IM, et al. Grim-19, a cell death regulatory gene product, is a subunit of bovine mitochondrial nadh:ubiquinone oxidoreductase (complex I). J Biol Chem. 2001; 276:38345–38348. [PubMed: 11522775]
66. Lazarou M, McKenzie M, Ohtake A, Thorburn DR, Ryan MT. Analysis of the assembly profiles for mitochondrial- and nuclear-DNA-encoded subunits into complex I. Mol Cell Biol. 2007; 27:4228–4237. [PubMed: 17438127]
67. McKenzie M, Ryan MT. Assembly factors of human mitochondrial complex I and their defects in disease. IUBMB Life. 2010; 62:497–502. [PubMed: 20552642]
68. Brockmann C, et al. The oxidized subunit B8 from human complex I adopts a thioredoxin fold. Structure. 2004; 12:1645–1654. [PubMed: 15341729]

69. Keeney PM, Xie J, Capaldi RA, Bennett JP Jr. Parkinson's disease brain mitochondrial complex I has oxidatively damaged subunits and is functionally impaired and misassembled. J neuroscience. 2006; 26:5256–5264. [PubMed: 16687518]

70. Abdrakhmanova A, Zwicker K, Kerscher S, Zickermann V, Brandt U. Tight binding of NADPH to the 39-kDa subunit of complex I is not required for catalytic activity but stabilizes the multiprotein complex. Biochim Biophys Acta. 2006; 1757:1676–1682. [PubMed: 17046710]

71. Ciano M, Fuszard M, Heide H, Botting CH, Galkin A. Conformation-specific crosslinking of mitochondrial complex I. FEBS Lett. 2013; 587:867–872. [PubMed: 23454639]

72. Angerer H, et al. The LYR protein subunit NB4M/NDUFA6 of mitochondrial complex I anchors an acyl carrier protein and is essential for catalytic activity. Proc Natl Acad Sci USA. 2014; 111:5207–5212. [PubMed: 24706851]

73. Ushakova AV, Duarte M, Vinogradov AD, Videira A. The 29.9 kDa subunit of mitochondrial complex I is involved in the enzyme active/de-active transitions. J Mol Biol. 2005; 351:327–333. [PubMed: 16005890]

74. Haack TB, et al. Mutation screening of 75 candidate genes in 152 complex I deficiency cases identifies pathogenic variants in 16 genes including NDUFB9. J med genetics. 2012; 49:83–89. [PubMed: 22200994]

75. Yip CY, Harbour ME, Jayawardena K, Fearnley IM, Sazanov LA. Evolution of respiratory complex I: “supernumerary” subunits are present in the alpha-proteobacterial enzyme. J Biol Chem. 2011; 286:5023–5033. [PubMed: 21115482]

76. Finel M, Skehel JM, Albracht SP, Fearnley IM, Walker JE. Resolution of NADH:ubiquinone oxidoreductase from bovine heart mitochondria into two subcomplexes, one of which contains the redox centers of the enzyme. Biochemistry. 1992; 31:11425–11434. [PubMed: 1332758]

77. Sheftel AD, et al. Human ind1, an iron-sulfur cluster assembly factor for respiratory complex I. Mol Cell Biol. 2009; 29:6059–6073. [PubMed: 19752196]

78. Vogel RO, et al. Identification of mitochondrial complex I assembly intermediates by tracing tagged NDUFS3 demonstrates the entry point of mitochondrial subunits. J Biol Chem. 2007; 282:7582–7590. [PubMed: 17209039]

79. Hirst J, Carroll J, Fearnley IM, Shannon RJ, Walker JE. The nuclear encoded subunits of complex I from bovine heart mitochondria. Biochim Biophys Acta. 2003; 1604:135–150. [PubMed: 12837546]

Europe PMC Funders Author Manuscripts

Europe PMC Funders Author Manuscripts

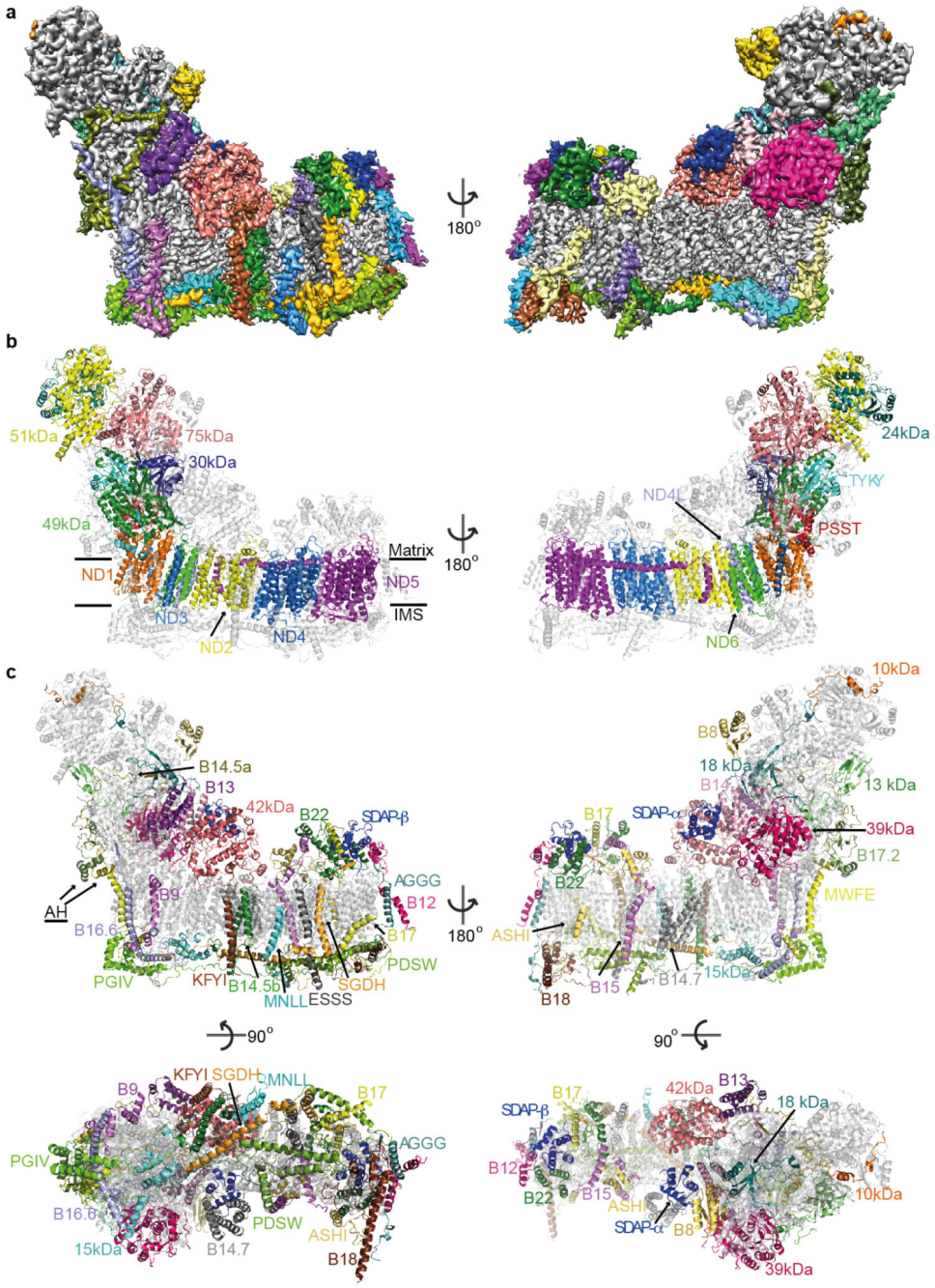

Figure 1. Structure of ovine complex I.

a. Cryo-EM density coloured by subunit, with core subunits in grey (left-right view). **b.** Structure depicted as a cartoon, with core subunits coloured and labelled, and supernumerary in grey and transparent. Approximate lipid bilayer boundaries are indicated. **c.** Structure depicted with core subunits in grey and supernumerary subunits coloured and labelled (left-right, matrix-IMS views). Amphipathic helices at the “back” of the complex, likely attached to the lipid bilayer, are indicated as AH.

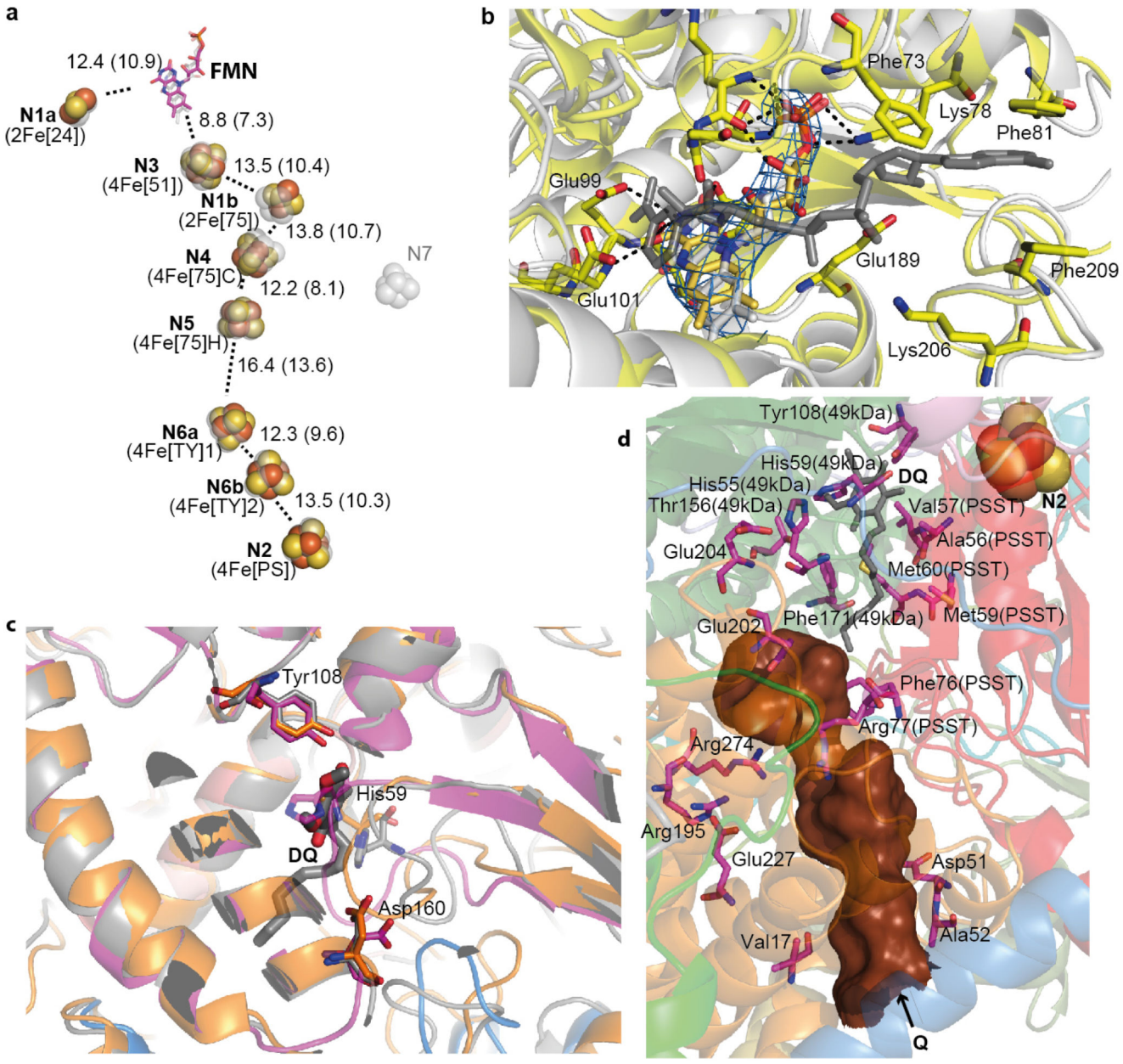

Figure 2. Arrangement of redox centers and substrate binding sites.

a. Fe-S clusters are shown as spheres with centre-to-centre and edge-to-edge (in brackets) distances indicated in Å, overlaid with transparent grey depictions from *T. thermophilus*. Both traditional and structure-based (in brackets) nomenclature for clusters is shown. **b.** NADH binding site (overlay with *T. thermophilus* structure in grey, containing NADH). Cryo-EM density for FMN is shown in blue. Key residues involved in interactions with FMN and NADH are shown as sticks. **c.** Quinone binding site with subunits coloured as Fig. 1. Key β1-β2$^{49\text{-kDa}}$ loop deviates from bacterial structure (grey) and is more similar to *Y. lipolytica* (orange, PDB 4WZ712), clashing with the decyl-ubiquinone (DQ) head group position in *T. thermophilus* (grey). **d.** Environment surrounding the Q cavity (brown surface,

entrance point indicated by an arrow), with some of functionally important residues shown as sticks and labelled with non-ND1 subunit names in brackets. The quinone from the aligned *T. thermophilus* structure is shown in grey (DQ), demonstrating that the distal part of the cavity is blocked in the ovine enzyme.

Europe PMC Funders Author Manuscripts

Europe PMC Funders Author Manuscripts

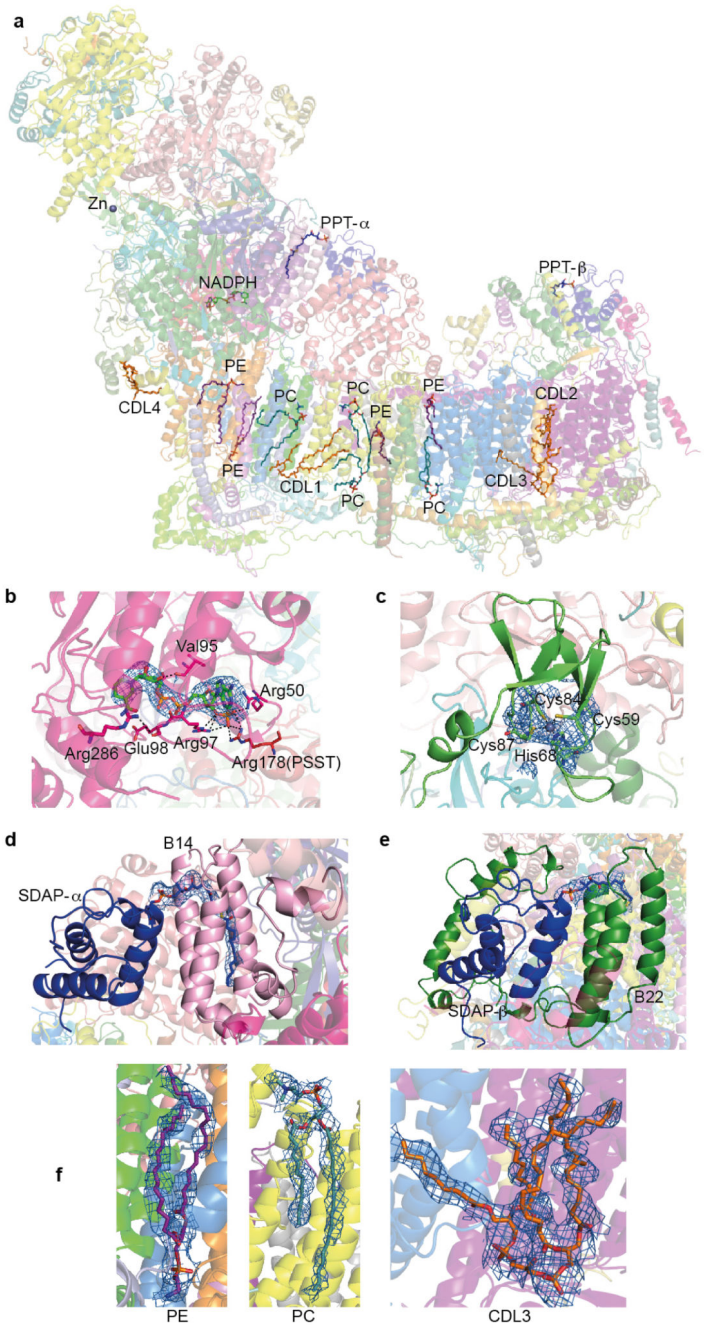

Figure 3. Additional cofactors identified in the structure.

a. Overview of the model coloured as in Fig. 1c, with cofactors shown as sticks and labeled as PPT for phosphopantetheine, CDL for cardiolipin, PC for phosphatidylcholine and PE for phosphatidylethanolamine. **b.** NADPH in the 39 kDa subunit. Interacting residues are shown. **c.** Zn^{2+} ion in the 13 kDa subunit, with coordinating residues. **d.** Phosphopantetheine in SDAP-α. **e.** Phosphopantetheine in SDAP-β. **f.** Lipids PE, PC and cardiolipin. All cofactors are shown with cryo-EM density carved to within 5 Å.

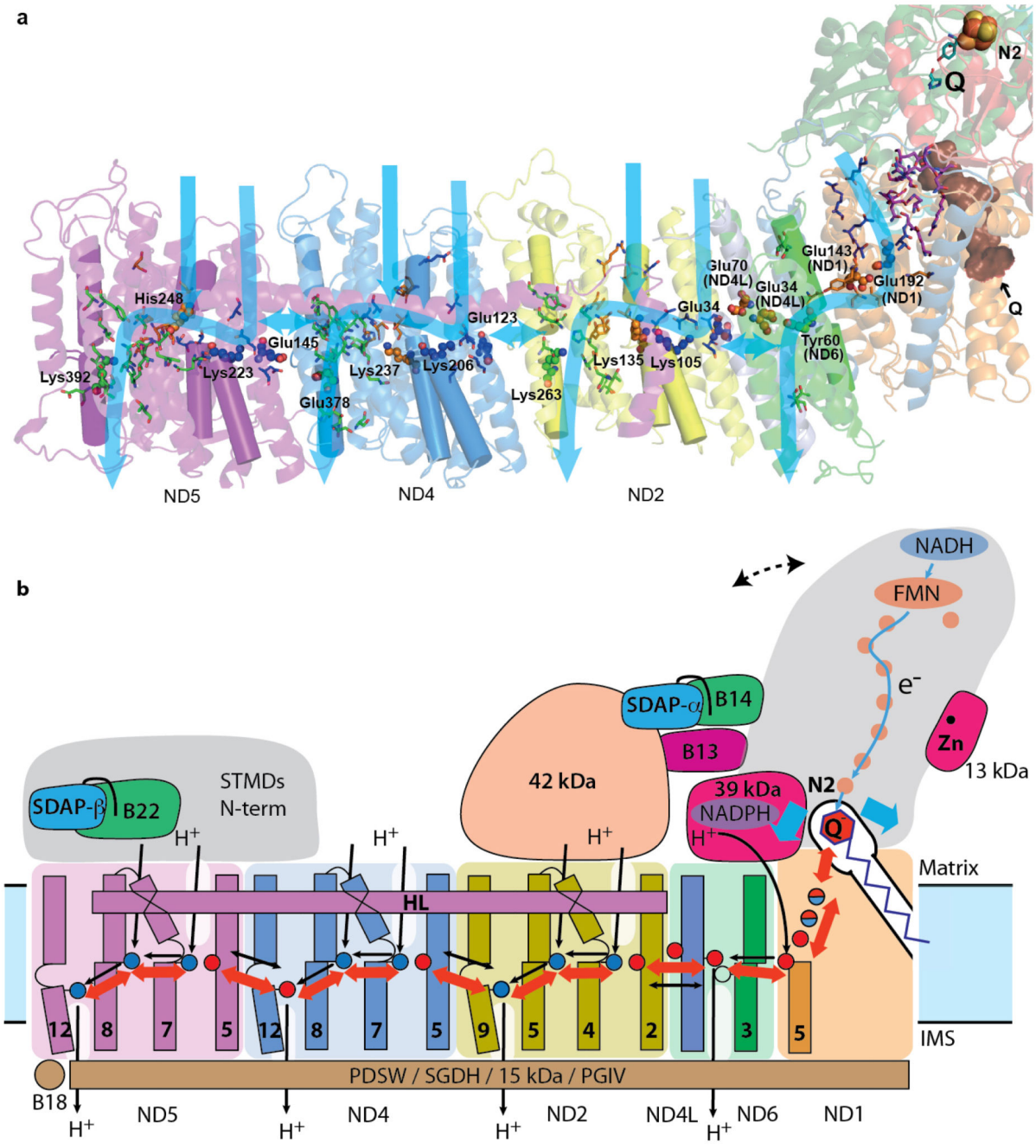

Figure 4. Mechanism of mitochondrial complex I.

a. Structure of the core subunits of ovine complex I coloured as in Fig. 1b, with polar residues in proton channels shown as sticks, with carbon in blue, orange and green for input, connecting and output parts respectively. Key residues GluTM5, LysTM7, Lys/HisTM8 and Lys/GluTM12 from the antiporters and the corresponding residues in the E-channel (near Q site) are shown as small spheres and labelled. These residues sit on flexible loops in discontinuous TM helices shown as cylinders. Polar residues linking the E-channel to the Q cavity (brown) are shown in magenta. Tyr108$^{49\text{-kDa}}$ and His59$^{49\text{-kDa}}$ are shown in cyan near

the position of bound Q in bacteria. Possible proton translocation pathways are indicated by blue arrows. **b.** Graphic of the coupling mechanism. Core and some putatively regulatory supernumerary subunits are shown. Conformational changes, indicated by red arrows, propagate from the Q site/E-channel to antiporter-like subunits via the central hydrophilic axis. Shifts of helices near the cluster N231 (blue arrows) may help initiate the process. ND5 helix HL and traverse helices from four supernumerary subunits on the IMS side may serve as "stators". Dashed line indicates the shift of peripheral arm in the "closed" conformation (Extended Data Fig. 8). NADPH-containing 39 kDa subunit and Zn-containing 13 kDa subunit are essential for activity and may serve as redox "sensors". Both SDAP subunits interact with their LYR partners *via* "flipped out" phosphopantetheine (black line). The net result of one conformational cycle, driven by NADH:ubiquinone oxidoreduction, is the translocation of four protons across the membrane (black lines indicate possible pathways).